3. GLOBAL OCEANS—M. L. Newlin and M. C. Gregg, Eds.

a. *Overview*—M. C. Gregg and M. L. Newlin

In 2013 the global oceans were characterized by a persistent pattern wherein saltier (higher evaporation) regions of the ocean surface continued to be anomalously salty and fresher (higher precipitation) regions continued to be anomalously fresh. The salt content in near-surface low latitude waters increased while intermediate waters formed at higher latitudes had decreased salt content. Notably, the South Pacific was fresher in 2013 compared to the long-term mean.

Global mean sea level (GMSL) continued to rise during 2013, on pace with a 20-year linear trend of 3.2 mm yr^{-1}. A portion of this trend (0.5 mm yr^{-1}) has been attributed to natural variability associated with the Pacific decadal oscillation (PDO; Hamlington et al. 2013), as well as ongoing contributions from the melting of glaciers and ice sheets and ocean warming (Rhein et al. 2013). Warming of the upper (0–700 m) oceans accounts for about 63% of the total increase in energy storage in the climate system from 1971 to 2010 (Rhein et al. 2013), and warming from 700 m depth to the ocean floor adds about another 30%. Melting ice and warming land account for about 3% each, and the warming atmosphere accounts for about 1% over those four decades.

The sea surface temperature anomaly (SSTA) was dominated by a negative PDO pattern in the North Pacific and by ENSO neutral conditions. The global ocean mean SSTA warmed by about 0.04°C compared with 2012, with the most warming in the North Pacific, which reached a historic high in 2013.

The substantial warming south of Bering Strait, Gulf of Alaska, and northeast Pacific (compared to 2012) appeared to be largely forced by atmospheric fluxes associated with a strong anomalous anticyclonic circulation near the Gulf of Alaska and a westerly surface wind anomaly in the northeast Pacific. This persistent high-pressure system promoted large-scale atmospheric subsidence farther to the south and altered the atmospheric flow pattern. As a result, the westerly winds in the North Pacific weakened significantly. The weakened winds reduced the rate of evaporation, leading to less latent heat loss from the ocean, which, in turn, caused the ocean warming. Ocean heat content also showed a warming trend in the western tropical Pacific and cooling trend in the eastern tropical Pacific from 1993 to 2013, consistent with overall trade-wind intensification during that time period. No large-scale equatorial surface current anomalies persisted for more than a month in the tropical Pacific basin compared to 2012. The annual average zonal current anomalies reveal a continuing northward shift of the Kuroshio Extension with a narrower and stronger annual signature.

Most of the subpolar North Atlantic warmed from 2012 to 2013 with the exception of parts of the Nordic Seas, which cooled. The observed meridional heat transport decrease in the full 8.5-year time series is likely due to interannual and decadal variability and the Gulf Stream shift southward back to its climatological position. Salinity increased in the upper 100 m of the North Atlantic with substantial freshening around 100–500-m depth (primarily north of 30°N). The Indian Ocean exhibited a widespread and significant warming trend in many regions; almost no regions had a statistically significant cooling trend.

Observations based on carbon system and pH measurements at ocean time-series stations in the North Atlantic and North Pacific indicate decreasing pH with rates ranging between -0.0014 yr^{-1} and -0.0024 yr^{-1}. Unlike previous years, the global phytoplankton distributions revealed that the relationship of decreasing Chl*a* with increasing SST was not equally prominent. In particular, regions of strong warming across the Pacific were often dominated by increases in Chl*a* though there is uncertainty in the current satellite record.

b. *Sea surface temperatures*—Y. Xue, Z. Hu, A. Kumar, V. Banzon, T. M. Smith, and N. A. Rayner

Sea surface temperatures (SST) play a key role in regulating climate and its variability by modulating air-sea fluxes and tropical precipitation anomalies. In particular, slow variations in SST such as those associated with the El Niño-Southern Oscillation (ENSO), Atlantic multidecadal oscillation (AMO), Pacific decadal oscillation (PDO), Indian Ocean dipole (IOD), and Atlantic Niño, are potential sources of predictability for climate fluctuations on timescales of a season and longer (Deser et al. 2010). A summary of global SST variations in 2013 is presented, with emphasis on the recent evolutions of ENSO and PDO, and also discussed with respect to the historical record since 1950.

To quantify uncertainties in SST variations, three SST datasets were used for this analysis: (1) the weekly Optimal Interpolation SST version 2 (OISST; Reynolds et al. 2002); (2) the Extended Reconstructed SST version 3b (ERSST; Smith et al. 2008); and (3) the (UK) Met Office Hadley Centre's sea ice and SST dataset (HadISST1; Rayner et al. 2003). The weekly OISST is a satellite-based analysis that uses in situ data for bias

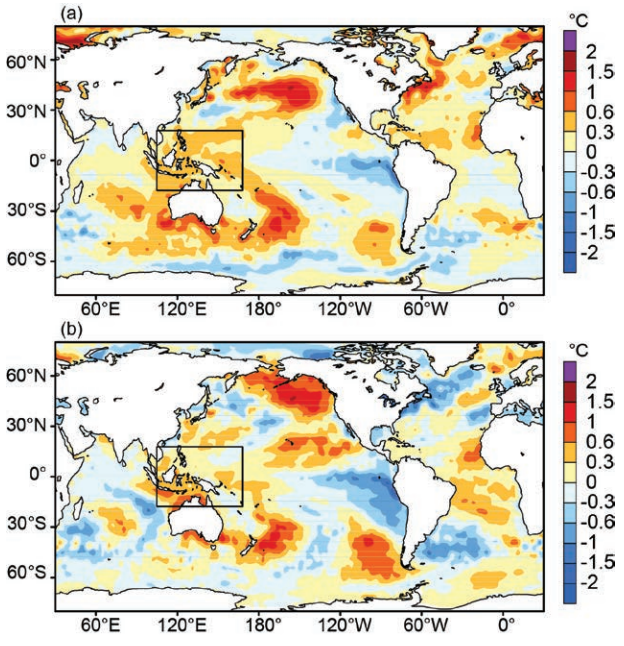

Fig. 3.1. (a) Yearly average OISST anomaly (°C, relative to 1981–2010 average) in 2013, (b) 2013 minus 2012 OISST anomaly. The box shows the area in which the normalized average SSTA is shown in Fig. 3.3a,b.

adjustments of the Advanced Very High Resolution Radiometer (AVHRR) data, and has been available since November 1981. The ERSST and HadISST1 are historical analyses beginning in the 19th century, and both use statistical procedures developed over the recent period to extend the SST analysis back in time when in situ observations were sparse. ERSST includes in situ data only, while HadISST1 includes both in situ measurements and AVHRR retrievals from 1982 onwards. Although ERSST and HadISST1 are among the best historical datasets, both involve bias corrections, tuning, and interpolations, which cause uncertainties, especially back to early periods of observations. The focus here is on intercomparison of the basin scale means among the three products, leaving regional differences among SST products to specific research publications. In this section, SST variations are quantified as SST anomalies (SSTAs) defined as departures from the 1981–2010 average (http://www.cpc.ncep.noaa.gov/products/people/yxue/sstclim).

The yearly mean SSTA in 2013 (Fig. 3.1a) was characterized by positive SSTA in the central North Pacific, Indo-Pacific warm pool (IPWP), and the North Atlantic and negative SSTA in the eastern equatorial Pacific (EPAC). The SSTA in the North Pacific resembled the negative phase of the PDO pattern (Mantua et al. 1997) and the normalized monthly PDO index averaged to be −1.2 in 2013. The SSTA in the Indo-Pacific was characterized by a dipole pattern with a positive center over IPWP and a negative center in EPAC. The average SSTA over IPWP, labeled as the box in Fig. 3.1, was more than +1 standard deviation (STD), while the SSTA average in EPAC was less than −0.5 STD.

The 2013 minus 2012 SSTA differences (Fig. 3.1b) show that there was a substantial warming south of Bering Strait, Gulf of Alaska, and northeast Pacific. The warming appeared to be largely forced by atmospheric fluxes associated with a strong anomalous anticyclonic circulation near the Gulf of Alaska and westerly surface wind anomaly in the northeast Pacific (see Fig. 3.9). There was a cooling in the southeast Pacific, along the east coast of North America, and subpolar North Atlantic. The tropical Atlantic was warmer in 2013 than in 2012.

The temporal evolution of seasonal mean SSTA in 2013 is shown in Fig. 3.2. The boreal winter

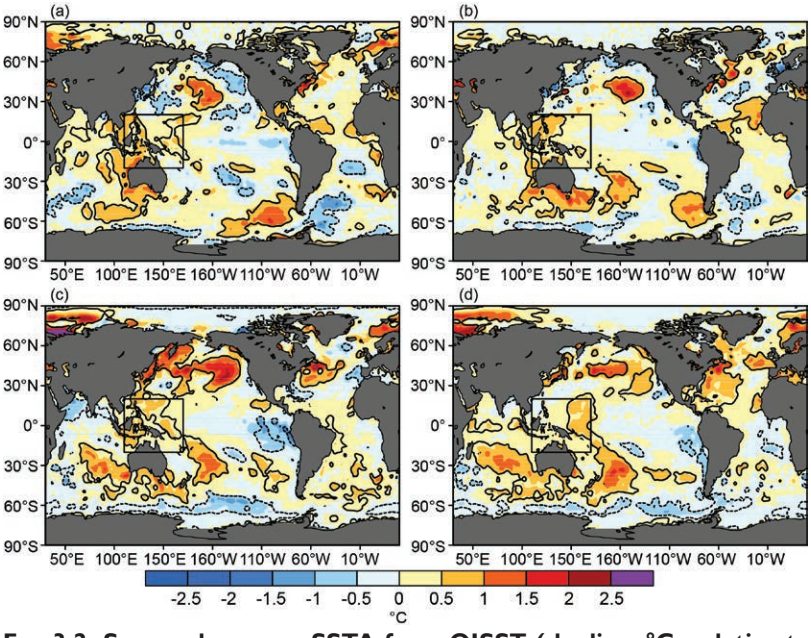

Fig. 3.2. Seasonal average SSTA from OISST (shading, °C, relative to 1981–2010 average) for (a) Dec 2012–Feb 2013, (b) Mar–May 2013, (c) Jun–Aug 2013, and (d) Sep–Nov 2013. The contours are +1 and -1 normalized seasonal average SSTA based on seasonally-averaged standard deviation over 1981–2010. The box shows the area in which the normalized average SSTA is shown in Fig. 3.3a,b.

2012/13 (December–February) was characterized by a negative PDO pattern in the North Pacific and ENSO-neutral conditions in the tropical Pacific [with definition of ENSO based on three-month running average of the NINO3.4 index with a threshold of +0.5°C (−0.5°C) for El Niño (La Niña); see section 4b for details]. Both ENSO-neutral and negative PDO conditions persisted throughout 2013 (see NINO3.4 and PDO indices in Fig. 3.3a,c). The positive SSTA over IPWP exceeding +1 STD persisted throughout 2013. Negative SSTA of more than −1 STD emerged in the eastern Pacific during summer and persisted into fall 2013. The SSTA in the North Atlantic was mostly positive during 2013.

To further understand the persistent positive SSTA over IPWP, the normalized monthly SSTA average was calculated in the box labeled in Fig. 3.1, referred to as Indo-Pacific warm pool SSTA (WSSTA). Figure 3.3a shows that WSSTA exceeded +1 STD during most of 2013 and 2010, in contrast to 2011 and 2012 when WSSTA was less than 0.5 STD. The time series since 1982 (Fig. 3.3b) shows that WSSTA (shading) was mostly negative before 1999 and positive after 1999. The sudden warming over IPWP is related to a multidecadal shift that happened around 1999 (Lyon et al. 2013). WSSTA is generally out-of-phase with NINO3.4 with a correlation −0.45 for the period 1982–2013. However, the correlation between WSSTA and NINO3.4 was −0.53 before 1999 and −0.31 after 1999. The weakened out-of-phase relationship between WSSTA and NINO3.4 after 1999 is probably related to the weakened ENSO variability after 1999 (Hu et al. 2013). In addition, the multidecadal shift around 1999 also contributes to the weakened relationship. The persistent positive WSSTA after 1999 likely forces persistent La Niña-like atmospheric circulations with enhanced convections over Indonesia and suppressed convections near the dateline. This was the case in 2013 (see http://www.cpc.ncep.noaa.gov/products/GODAS).

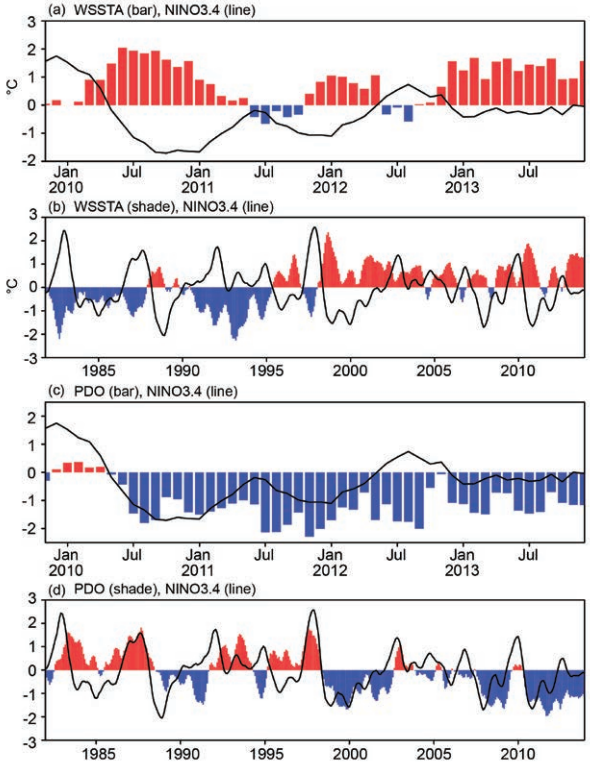

Fig. 3.3. (a) Monthly normalized average SSTA (°C) over Indo-Pacific warm pool in the box shown in Fig. 3.2, labeled as WSSTA (bar) and monthly normalized NINO3.4 index (average SSTA in 170°–120°W, 5°S–5°N; line) for 2010–13 and (b) 5-month running mean of SSTA indices (°C) for 1982–2013; SSTA is relative to 1981–2010 average. (c) Monthly normalized PDO index (bar) and NINO3.4 index (line) for 2010–13 and (d) 5-month running mean of PDO and NINO3.4 index for 1982–2013.

The connection between the ENSO cycle and PDO is further explored. The PDO index is defined as the standardized time series of the projection onto the 1st empirical orthogonal function (EOF) of monthly ERSST in the North Pacific north of 20°N during the period 1900–93 following the approach of Mantua et al. (1997). There was a switch from positive to negative PDO around June 2010 which coincided with the onset of the 2010/11 La Niña (Fig. 3.3c). This negative PDO phase has persisted since that time. The time series for 1982–2013 (Fig. 3.3d) shows that negative PDO tends to be in phase with, but lasts longer than, La Niña. In addition, there was a regime shift of PDO around 1999. After 1999 negative PDO was more frequent than the positive PDO, while before 1999 positive PDO was more frequent. The correlation between monthly PDO and NINO3.4 at zero lag is 0.42 in 1982–2013, while it is 0.38 in 1982–98 and 0.51 in 1999–2013. The higher correlation since 1999 is partly attributed to the fact that both the PDO and NINO3.4 were in prevalent negative phases since 1999.

The historical perspective of the yearly mean SSTA in 2013 was next investigated. Figure 3.4 shows the average SSTAs in the (a) tropical Pacific, (b) tropical Indian Ocean, (c) tropical Atlantic, (d) North Pacific, (e) North Atlantic, and (f) global ocean. The SSTA time series of OISST are largely consistent with ERSST in the common period 1982–2013. HadISST also agrees well with OISST and ERSST except it is generally cooler in the tropical Indian Ocean, where the differences reach up to 0.2°C.

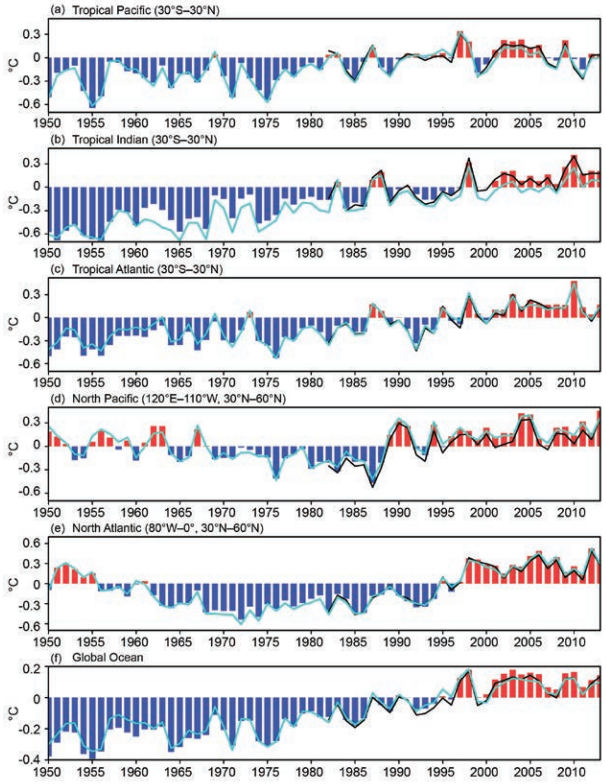

Fig. 3.4. Yearly mean SSTA (°C, relative to 1981–2010 average) from ERSST, and HadISST (blue line) for 1950–2013 (bar) and OISST for 1982–2013 (black line) averaged over the (a) tropical Pacific, (b) tropical Indian Ocean, (c) tropical Atlantic, (d) North Pacific, (e) North Atlantic, and (f) global ocean.

The mean SSTA in the global ocean was dominated by a warming trend superimposed with interannual variations largely associated with El Niño and La Niña events (Fig. 3.4f). For example, the peaks and valleys in the global ocean SSTA often correspond with those in the tropical Pacific SSTA (Fig. 3.4a). The global ocean SSTA warmed by about 0.04°C (Fig. 3.4f). After a 30-year period (1970–99) of a warming trend in the global ocean SST (+0.11°C decade^{-1} in ERSST and +0.06°C decade^{-1} in HadISST), the past decade in 2000–13 had little further trend (+0.007°C decade^{-1} in ERSST and +0.02°C decade^{-1} in HadISST) .

The tropical Indian Ocean SSTA is dominated by an upward trend with an increase of 0.9°C from 1950 to 2010 when the historical high value was reached (Fig. 3.4b). The interannual variations in the tropical Indian Ocean SSTA correspond well with those in the tropical Pacific SSTA due to the remote influences of ENSO. In the tropical Atlantic, SSTA was mostly negative before 1995, and warmed significantly from −0.43°C in 1992 to +0.31°C in 2003. The positive SSTA largely persisted from 2003 to 2009, then suddenly increased to the historical high value +0.46°C in 2010 (Fig. 3.4c), due to the combined influences of El Niño, long-persistent negative phase of NAO, as well as the long-term trend (Hu et al. 2011). Since 2010, the tropical Atlantic SST has cooled down substantially. The North Pacific SSTA trended downward from 1950 to 1987, but rebounded from −0.5°C in 1987 to 0.31°C in 1990, and has been persistently positive since then (Fig. 3.4d). The North Pacific SSTA increased 0.27°C from 2012 to 2013, and reached a historical high in 2013. The North Atlantic SSTA trended downward from 1951 to early 1970s, and then trended upward, reaching a peak value in 2006. From 2006 to 2010, the SSTA had a downward trend, but rebounded and reached a historical high in 2012 (Fig. 3.4e). There was a cooling of −0.21°C from 2012 to 2013.

c. Ocean heat content—G. C. Johnson, J. M. Lyman, J. K. Willis, T. Boyer, J. Antonov, S. A. Good, C. M. Domingues, and N. Bindoff

Storage and transport of heat in the ocean are central to aspects of climate such as ENSO (Roemmich and Gilson 2011), tropical cyclones (Goni et al. 2009), sea level rise and the global energy budget (Church et al. 2011), constraining global warming scenarios (Otto et al. 2013), and melting of ice sheet outlet glaciers around Greenland (Straneo and Heimbach 2013) and the Antarctic (Rignot et al. 2013).

An estimate of upper (0–700 m) ocean heat content anomaly (OHCA) for 2013 (Fig. 3.5a) is computed from a combination of in situ ocean temperature data and satellite altimetry data (hereafter referred to as the combined estimate). In situ data are from (UK) Met Office Hadley Center EN3 V2a (Ingleby and Huddleston 2007), derived mostly from the World Ocean Database (Boyer et al. 2009), but with a January 2014 download of Argo (Roemmich et al. 2009) data. Updated mechanical and expendable bathythermograph (MBT and XBT) bias corrections from Ishii and Kimoto (2009) are applied, along with a statistical quality control (Lyman and Johnson 2014). Since OHCA changes are related to depth-integrated ocean temperature changes, increases in OHCA are sometimes referred to here as warming and OHCA decreases as cooling. Some of the data used in this analysis are preliminary, pending delayed-mode scientific quality control; however, strong regional signals are unlikely to change upon data finalization.

Upper OHCA in 2013 (Fig. 3.5a) shows typical eddy and meander signatures (Johnson et al. 2012a). Similarly, differences of upper OHCA between 2013

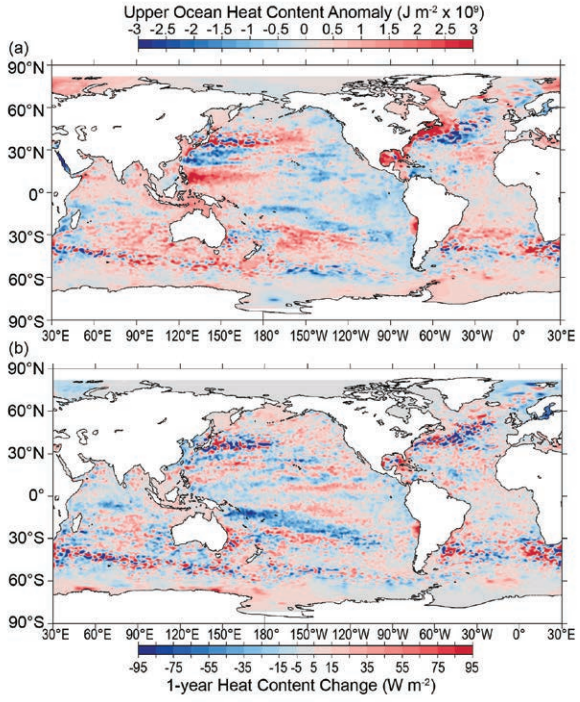

Fig. 3.5. (a) Combined satellite altimeter and in situ ocean temperature data estimate of upper (0–700 m) ocean heat content anomaly (OHCA; ×10⁹ J m⁻²) for 2013 analyzed following Willis et al. (2004), but using an Argo monthly climatology and displayed relative to a 1993–2013 average. (b) The difference of 2013 and 2012 combined estimates of OHCA expressed as a local surface heat flux equivalent (W m⁻²). For panel comparisons, note that 95 W m⁻² applied over one year results in a 3 × 10⁹ J m⁻² change of OHCA.

and 2012 (Fig. 3.5b) exhibit typical interannual variability. OHCA variability (and net increases) are also found from 700 to 2000 m in depth (Levitus et al. 2012) and even in the abyssal ocean below (Purkey and Johnson 2013). These variations, as well as salinity and mass signals, all contribute to local sea level anomalies (Leuliette and Willis 2011). Despite these additional factors, there are many large-scale visual similarities between the combined estimate of upper OHCA (Fig. 3.5a) and sea level (see Fig. 3.28a) fields in 2013. This similarity reflects mostly the large contribution of upper OHCA variations to sea level variations (Church et al. 2010), but also to a lesser extent the influence of the altimeter data in the combined estimate (Willis et al. 2004).

Large-scale patterns are evident in the combined estimate of upper OHCA for 2013 (Fig. 3.5a) and its difference from 2012 (Fig. 3.5b). The pattern of annual mean OHCA (Fig. 3.5a) on the equator in the Pacific exhibits slightly cool values in the east and slightly warm values in the west. This relatively neutral pattern is consistent with the persistence of near-neutral conditions for ENSO in the Pacific from 2012 through 2013 (section 4b).

In 2013, the North Pacific (Fig. 3.5a) showed a pattern of anomalous warmth in the central Pacific and cold in the eastern Pacific that is typical of the negative phase of the Pacific decadal oscillation (PDO; Mantua et al. 1997), although this pattern was weaker in 2013 than in 2012. Extratropical SST anomalies in 2013 exhibited a similar pattern (see Fig. 3.1). South of the Kuroshio Extension in the western Pacific there was a cool patch between 20° and 30°N that contrasts with the anomalously warm patch to the south that extended well east of the Philippines. There were strong zonal surface current anomalies co-located with these two features (see Fig. 3.17a).

In the South Pacific, the strong band of cooling from 2012 to 2013 (Fig. 3.5b) that extended from east of the Solomon Islands to about 30°S, 100°W is associated with an increase in eastward tendency of surface velocity (see Fig. 3.17b) and an increase in Ekman suction (anomalous upwelling) owing to changes in the winds (see Fig. 3.9b). This cooling broke up a band of anomalously warm upper OHCA in the South Pacific extending from the Solomon Islands in the west to about 30°S, 100°W (Fig. 3.5a) that had been present at various latitudes since 2006 (Johnson et al. 2013a; previous *State of the Climate* reports). However, much of the South Pacific south of the Tropic of Capricorn (~23°S) remained anomalously warm in 2013.

Upper OHCA in the Indian Ocean remained mostly warm in 2013 (Fig. 3.5a) compared to the 1993–2013 average, with a prominent cool patch in the southern half of the Mozambique Channel, where strong cooling occurred between 2012 and 2013 (Fig. 3.5b). Cooling from 2012 to 2013 in a band around 8°S is associated with an increase in eastward flow to the north and westward flow to the south (see Fig. 3.17b), consistent with an increase in the strength of the thermocline ridge at that latitude and an increase in Ekman suction just south of the equator extending westward from Indonesia (see Fig. 3.9b).

Much of the subpolar North Atlantic warmed from 2012 to 2013 (Fig. 3.5b), although some of the Nordic Seas cooled. With these changes, in this region a small portion of the Irminger Sea and some patches west of Norway remained colder than average in 2013 (Fig. 3.5a). In 2013, as in 2012 (Johnson et al. 2013a), there was a meridional dipole of OHCA along the Gulf Stream extension, warm to the northwest and cool to the southeast. The tropical Atlantic mostly warmed from 2012 to 2013 (Fig. 3.5b); hence it remained

warmer than the 1993–2013 average, with some cool patches along the tropical cyclone path from Africa to the Antilles (Fig. 3.5a).

A few distinct (Fig. 3.6a) and statistically significant (Fig. 3.6b) regional patterns stand out in the 1993–2013 local linear trends of upper OHCA. In the Indian Ocean, the warming trend is widespread and statistically significant in many locations, with almost no regions of statistically significant cooling trends in that ocean.

In the Atlantic Ocean, the Labrador, western Irminger, and Nordic Seas have all trended warmer over 1993–2013 (Fig. 3.6a), reflecting a robust regional warming trend over the interval (Fig. 3.6b). These changes may result from changes in the wind stress curl linked to changes in Atlantic multidecadal variability (AMV) since 1993 (Häkkinen et al. 2013). Eastern portions of the subtropical Atlantic and most of the tropics also trend warmer across both hemispheres. Statistically significant cooling trends in the Atlantic are limited to the Gulf Stream extension,

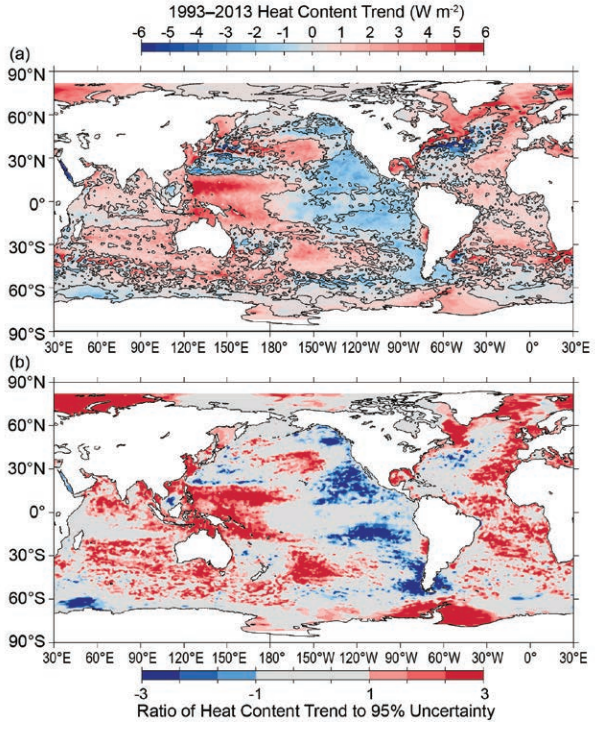

Fig. 3.6. (a) Linear trend from 1993–2013 of the combined satellite altimeter and in situ ocean temperature data estimate of upper (0–700 m) ocean heat content anomaly OHCA (W m^{-2}) analyzed following Willis et al. (2004) but relative to a monthly Argo climatology. Areas with statistically significant trends are outlined in black. (b) Signed ratio of the linear trend to its 95% uncertainty estimate, with increasing color intensity showing regions with increasingly statistically significant trends.

probably related to a southward shift in that current over the past few years. This shift is expected with an overall declining NAO index (Pérez-Hernández and Joyce 2014), but recent subtropical cooling has also been linked to a reduction in the Atlantic meridional overturning circulation (Cunningham et al. 2013).

Statistically significant (Fig. 3.6b) 1993–2013 regional trends in the Pacific Ocean (Fig. 3.6a) include warming in the western tropical Pacific and extra-equatorial cooling in the east, consistent (via the geostrophic relation) with general strengthening of the interior subtropical-tropical circulation attributed to trade wind intensification (Merrifield et al. 2012). The statistically significant warming in the central North Pacific and cooling south of Alaska and off the west coast of North America are also consistent with an overall downward trend in the PDO index since 1993. There is a similar trend pattern in the South Pacific.

The overall 1993–2013 trends in Southern Ocean upper OHCA are towards warming, consistent with previous analyses (Böning et al. 2008), but with some cooling trends in localized regions, most notably around South America (Fig. 3.6a). The apparent trends adjacent to Antarctica are located in both in situ and altimeter data-sparse regions and may not be as robust as suggested by the statistics (Fig. 3.6b).

Warming of the upper (0–700 m) oceans accounts for about 63% of the total increase in energy storage in the climate system from 1971 to 2010 (Rhein et al. 2013), and warming from 700 m depth to the ocean floor adds about another 30%. Melting ice and warming land account for about 3% each, and the warming atmosphere accounts for about 1% over those four decades.

Four different upper ocean estimates of globally-integrated in situ OHCA (Fig. 3.7) reveal a large increase in global integrals of that quantity since 1993. While each of the curves appears to show interannual to decadal variability in upper ocean heat content, they do not always agree in the details (Abraham et al. 2013; Church et al. 2013). These details differ for a variety of reasons including differences in climatology and base period, treatment of the seasonal cycle, mapping methods, instrument bias corrections, quality control, and other factors (Lyman et al. 2010). Some of these factors are not taken into account in some of the displayed uncertainties, and the offsets applied to the curves for display are arbitrary. Uncertainties in annual estimates of global upper OHCA only permit statistically significant trends to be estimated over about 10 years or longer (Lyman 2012).

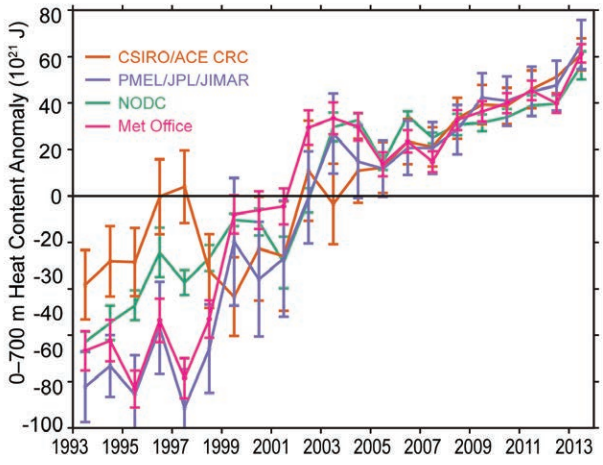

FIG. 3.7. Time series of annual average global integrals of in situ estimates of upper (0–700 m) OHCA (× 10^{21} J, or ZJ) for 1993–2013 with standard errors of the mean. The CSIRO/ACE CRC estimate (http://www.cmar.csiro.au/sealevel/thermal_expansion_ocean_heat_timeseries.html) and its uncertainties are updated following Domingues et al. (2008), except without a 3-year running filter applied. The PMEL/JPL/JIMAR estimate assumes a representative average (Lyman and Johnson 2014) using data and instrument bias corrections described in the text with uncertainty estimate methodology following Lyman et al. (2010). The NODC estimate (http://www.nodc.noaa.gov/OC5/indprod.html) follows Levitus et al. (2012). Uncertainties are estimated solely from the variance of quarterly estimates of OHCA. The (UK) Met Office estimate is computed from gridded monthly temperature anomalies (relative to 1950–2013) calculated from EN4.0.2 (Good et al. 2013) data following Palmer et al. (2007). An updated version of the instrument bias corrections of Gouretski and Reseghetti (2010) was applied. Uncertainty estimates follow Palmer and Brohan (2011). For comparison, all estimates have been individually offset (vertically on the plot), first to their individual 2004–13 averages (the best sampled time period), and then to their collective 1993–2013 average (the record length).

The rate of heat gain from linear trends fit to each of the global integral estimates from 1993 through 2013 (Fig. 3.7) are 0.29 (±0.12), 0.48 (±0.13), 0.34 (±0.09), and 0.42 (±0.25) W m^{-2} applied over Earth's surface area (5.1 × 10^{14} m^2) for the CSIRO/ACE CRC, PMEL/JPL/JIMAR, NODC, and (UK) Met Office estimates, respectively. These trends are all statistically different from zero and agree within their quoted 5% to 95% range of uncertainty. The uncertainty estimates for the trends are based on the residuals, taking their temporal correlation into account when estimating of the degrees of freedom (Von Storch and Zwiers 1999).

d. Ocean surface heat and momentum fluxes—L. Yu, X. Jin, P. W. Stackhouse Jr., Y. Xue, and A. Kumar

The net heat flux (Q_{net}) at the ocean surface is the sum of solar radiation (SW), longwave radiation (LW), turbulent latent heat (LH), and sensible heat (SH) fluxes. The balance of these heat exchange processes is fundamental to the understanding of the role of the ocean in mitigating radiative perturbations and modulating the global climate. Global maps of surface heat fluxes and winds are now being produced from satellite observations and by incorporating outputs of numerical weather prediction models as supplemental datasets. The net heat flux presented here is a combination of surface fluxes produced by two flux projects. One is the Objectively Analyzed air-sea Fluxes (OAFlux) project (http://oaflux.whoi.edu) at the Woods Hole Oceanographic Institution (Yu and Weller 2007; Yu et al. 2008) that provides turbulent LH and SH estimates from using an optimal blending of flux-related variables from satellite retrievals and atmospheric reanalyses. The other project is the CERES (Clouds and Earth's Radiant Energy Systems) Fast Longwave And Shortwave Radiative Fluxes (FLASHFlux) project (http://flashflux.larc.nasa.gov) at the NASA Langley Research Center (Stackhouse et al. 2006; Kratz et al. 2014) that delivers global daily surface SW and LW flux products in near real-time (within 1 week). The OAFlux project has recently expanded to the global analysis of daily 10-m vector wind fields through synthesizing satellite radiometers and scatterometers (Yu and Jin 2012, 2014, manuscript submitted to *J. Geophys. Res.*). The wind-driven ocean circulation is a major mechanism for redistributing solar heating over the global oceans and contributes to much of the change observed in heat content (see Fig. 3.5), ocean salinity (see Fig. 3.11), sea level (see Fig. 3.28), and ocean surface currents (see Fig. 3.17).

The annually-averaged Q_{net} in 2013 is displayed in Fig. 3.8a, showing that the maximum ocean heat gain (>120 W m^{-2}) is associated with the equatorial cold tongues, and the maximum ocean heat loss (<140 W m^{-2}) with the western boundary currents (WBCs) regimes. Compared to 2012 (Fig. 3.8b), Q_{net} in 2013 had an enhanced net heat loss (negative difference anomalies) over the Atlantic basin and an enhanced net heat gain (positive difference anomalies) over the Pacific basin and the subtropical south Indian Ocean. In the North Atlantic Ocean, the net heat loss anomalies exceeded 20 W m^{-2} both north of 30°N and in the tropical latitudes. Sandwiched between the two regions of heat loss (negative) anomalies is a narrow latitudinal band of weak positive difference anomalies, forming a tripole pattern

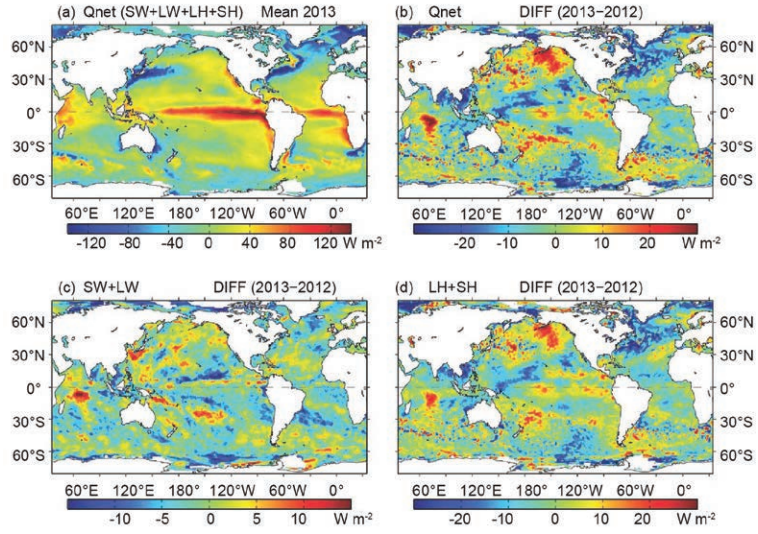

Fig. 3.8. (a) Annual average net heat flux into the ocean (Q_{net}) in 2013. Positive (negative) values denote ocean heat gain (loss). (b) Annual average difference in Q_{net} between 2013 and 2012. (c) and (d) are the 2013 – 2012 difference anomalies in surface radiation (SW + LW) and turbulent heat fluxes (LH + SH), respectively. In (b)–(d), positive (negative) anomalies denote ocean gains (losses) of heat in 2013 compared to 2012. (Source: SW/LW produced by FLASHFlux and LH/SH by OAFlux.)

of Q_{net} difference anomalies. The pattern is shown in both surface net radiation SW + LW (Fig. 3.8c) and turbulent LH + SH (Fig. 3.8d) difference anomalies, with the magnitude of the latter being about five times larger than that of the former. The occurrence of the difference pattern was in close association with the atmospheric conditions of a predominantly positive NAO phase in 2013 (see Fig. 3.4).

In sharp contrast to the North Atlantic, much of the North Pacific Ocean in 2013 experienced an enhanced oceanic heat gain (positive anomalies), with the central basin and the Gulf of Alaska the center of intensive heating (>20 W m^{-2}). SSTs in these two areas increased by more than 1°C (see Fig. 3.1). The close association of the surface warming with the abnormally high net heat input is a clear indication that the extra heating received at the ocean surface contributed to the increase of local SST. In 2013, near-surface atmospheric circulation in the North Pacific was dictated by a persistent high-pressure system centered over the Gulf of Alaska, which promoted large-scale atmospheric subsidence farther to the south and altered the atmospheric flow pattern. As a result, the westerly winds in the North Pacific weakened significantly (Fig. 3.9a). The weakened winds reduced the rate of evaporation, leading to less latent heat loss from the ocean (Fig. 3.8d), which, in turn, caused the ocean warming. The negative PDO phase, which began in May 2010, continued to be negative in 2013 (see Fig. 3.2). The relationship between the PDO phase and the persistent high-pressure system over the Gulf of Alaska is not currently known.

The net heat flux appears to have also contributed to the change in SST anomalies in the tropical Indian Ocean. Enhanced net heating was observed in the south central Indian Ocean due to both increased downward radiation and decreased latent and sensible heat fluxes in response to the weakened wind speed (Fig. 3.9a). Correspondingly, SST in the area increased by more than 1°C in 2013 (see Fig. 3.1). Yet, not all SST anomalies were induced by Q_{net}. For instance, the SST in the eastern tropical Pacific decreased by more than 1°C in 2013, but the net heat input in the region was increased by more than 20 W m^{-2} in the same pe-

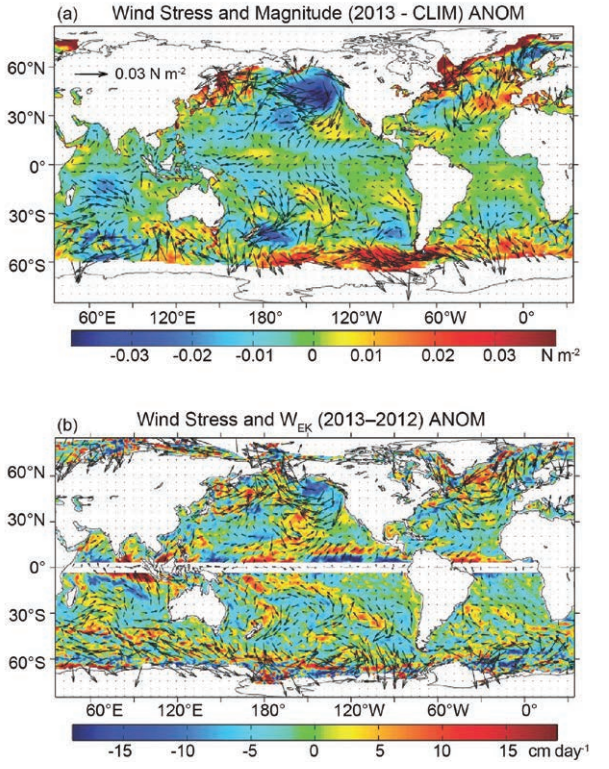

Fig. 3.9. (a) The 2013 wind stress magnitude anomalies (colored background) superimposed with vector anomalies from OAFlux. The 25-year (1988–2012) average was used to compute the anomalies. (b) The 2013 – 2012 difference anomalies in Ekman vertical velocity (w_{EK}, unit: cm day^{-1}; colored background) and wind stress (vectors). Positive (negative) values denote upwelling (downwelling) anomalies.

riod. In fact, the increase of Q_{net} was a response to the cooler SST, as the latter led to less latent heat loss from the ocean (Fig. 3.8d) and hence, more net downward heat flux. In the tropics, it is known that ENSO SSTs are governed more by ocean dynamics through wind-driven upwelling of cold water from the thermocline (Wyrtki 1981). This SST-LH-Q_{net} relationship, which was apparently at work in 2013, implies that Qnet has acted as a damping mechanism to the existing SST anomalies, suppressing the growth of ENSO SSTs. The changing relationships between Q_{net} and SST from one basin to another demonstrate that the global climate system is influenced by intricate feedbacks between the ocean and the atmosphere.

The changes of the 2013 wind stress relative to the 1988–2012 average and the 2012 condition are shown in Fig. 3.9a,b, respectively. The anomaly pattern associated with the persistent high-pressure system over the Gulf of Alaska was the most noted pattern in 2013. The near-surface atmospheric circulation was altered, which weakened the westerly winds over the North Pacific significantly. Aside from the North Pacific, weakened winds were observed in the southeast trades over the south Indian Ocean and also on the northern edge of Southern Hemisphere (SH) westerlies over the 30°–50°S latitudinal band. By contrast, the southern edge of SH westerlies, strengthened considerably in the Pacific and Atlantic sectors.

The spatial variations of wind stress cause divergences and convergences of the Ekman transport, leading to a vertical velocity, denoted Ekman pumping velocity w_{EK}, at the base of the Ekman layer. The convergent flow drives downwelling and the divergent flow drives upwelling from beneath. This pattern of vertical motion brings the interior of the ocean into motion and sets the wind-driven gyre circulation. Computation of w_{EK} follows the equation: $w_{EK} = 1/\rho\Delta\times(\tau/f)$, where ρ *is* the density and f the Coriolis force. Figure 3.9b shows the 2013 – 2012 w_{EK} difference anomalies with superimposition of the difference anomalies of surface wind stress vectors. It is evident that the Ekman pumping in the central North Pacific and the Gulf of Alaska enhanced significantly (negative anomalies) in 2013, in relation to the weakening of the westerly winds associated with the high-pressure system stationed in the region. The changes of w_{EK} in the near-equatorial downwelling regions are also noted, with downwelling enhanced in the eastern Pacific sector (negative anomalies) but weakened in the central equatorial Pacific and Atlantic (positive anomalies). Changes at latitudes poleward of 60°S are also noticeable; the predominant negative difference anomalies suggest a weakening of the upwelling in the region.

Yearly variability of Q_{net} over the global oceans is dominated by LH + SH. The long-term perspective of the change in the 2013 LH + SH can be seen from the 1958–2013 annual time series of the globally-averaged LH + SH (Fig. 3.10a). The 2013 average value was slightly lower compared to 2012, continuing the downward trend that started around 2000. The tendency toward reversing the upward trend that dictated the decades of 1980s and 1990s holds strong. Since 1958, LH + SH showed a minimum at 99 W m^{-2} in 1977 and a maximum at 109 W m^{-2} in 1999, with LH being the major contributor. Yearly variability of the near-surface wind derived from satellite observations since 1988 is displayed in Fig. 3.10b, showing that the upward trend in the 1990s has leveled off since 1999 and the long-term tendency of the globally-averaged winds in the recent decade has remained steady.

The OAFlux winds have an averaged root-mean-square (rms) difference of 0.71 m s^{-1} in wind speed (9%) and 17° in wind direction when compared to more than 120 buoys (Yu and Jin 2012). The OAFlux heat flux analysis has an rms difference of 9.6 W m^{-2} (8%) for LH and 2.6 W m^{-2} (15%) for SH (Yu et al. 2008). The FLASHFlux has an rms error of 29.3 W

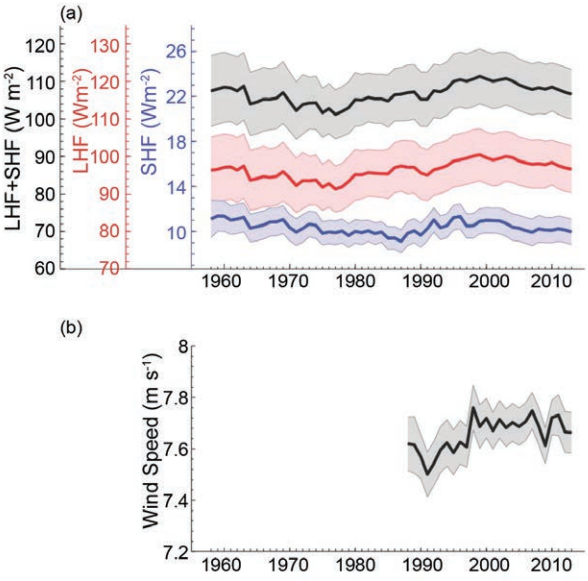

Fig. 3.10. (a) Year-to-year variations of global-averaged annual mean latent plus sensible heat flux (LHF + SHF; W m^{-2}, black curve), latent heat flux (LHF; W m^{-2}, red curve), and sensible heat flux (SHF; W m^{-2}, blue curve) from OAFlux. (b) Year-to-year variations of global-averaged annual mean wind speed (m s^{-1}) from OAFlux. The shaded areas indicate the error bars of the fluxes and wind speed estimates at the 95% confidence level.

m^{-2} (15.7%) for downward SW and 18.6 W m^{-2} (6.0%) for downward LW (Kratz et al. 2010). The FLASHFlux algorithm has been upgraded to version 3a from 2012 onward, with improvements most evident in the SW component. The fidelity of the OAFlux and FLASHFlux in 2013 was analyzed using the surface fluxes from the NCEP/Climate Forecast System Reanalysis (CFSR; Saha et al. 2010). There was an overall good agreement in LH and SH anomaly pattern, and also in Q_{net} because of the dominance of LH + SH over SW + LW in the Q_{net} anomalies. There were differences in the SW + LW anomalies between satellite and model products, albeit the broad-scale patterns were similar.

e. *Sea surface salinity*—G. C. Johnson, J. M. Lyman, G. S. E. Lagerloef, and H.-Y. Kao

Ocean storage and transport of freshwater are intrinsic to aspects of global climate, including the water cycle (e.g., Schanze et al. 2010), El Niño (e.g., Roemmich and Gilson 2011), and anthropogenic climate change (e.g., Held and Soden 2006). Since 2004, the achievement of near-global coverage by Argo (Roemmich et al. 2009) has allowed an annual assessment of upper ocean salinity and its complement, freshwater, usually measured within a few meters of the ocean surface. Although somewhat less accurate, the Aquarius satellite (http://aquarius.nasa.gov/index.html) has measured sea surface salinity (SSS) for the top cm of the global ocean with greater temporal and spatial resolution since August 2011. These two complementary data sources are used to examine annual and seasonal SSS variability, respectively.

The in situ data, downloaded from an Argo Global Data Assembly Center in January 2014, are a mix of real-time (preliminary) and delayed-mode (scientific quality-controlled). The estimates presented here could change after all data have been subjected to careful scientific quality control. Analysis procedures for Argo follow Johnson and Lyman (2012). For Aquarius, SSS release V2.8.1 swath data interpolated to 1° × 1° monthly maps with a bilinear fit and 150-km radius are used.

Climatological SSS patterns are correlated with surface freshwater flux—the sum of evaporation, precipitation, and river runoff (e.g., Schanze et al. 2010)—but advection and mixing are also important in many locations on seasonal (Yu 2011) and longer (Lagerloef et al. 2010) time scales. In each ocean basin, subtropical salinity maxima centered between roughly 20° and 25° in latitude (Fig. 3.11, gray contours) are signatures of the predominance of evaporation over precipitation. Conversely, in most regions where climatological surface salinities are relatively fresh, such as the high latitudes and the intertropical convergence zones (ITCZs), precipitation generally dominates over evaporation.

The 2013 SSS anomalies (Fig. 3.11a, colors) reveal some large-scale patterns that also hold from 2004 to 2013. The regions around the subtropical salinity maxima are generally salty with respect to World Ocean Atlas (WOA) 2009 (Antonov et al. 2010), except in the center of the South Pacific and in the eastern south Indian Ocean, where strong interannual variations, discussed below, disrupt that pattern. Most of the high-latitude climatologically fresh regions appear fresher overall than WOA 2009, including in the vicinity of much of the Antarctic Circumpolar Current near 50°S and in portions of the subpolar gyres of the North Pacific and Atlantic. These multiyear patterns are consistent with an increase in the hydrological cycle over the

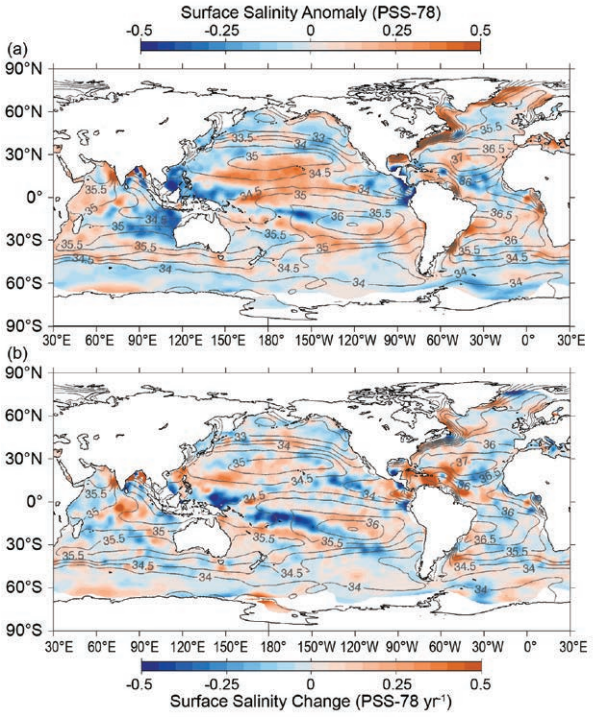

Fig. 3.11. (a) Map of the 2013 annual surface salinity anomaly estimated from Argo data (colors in PSS-78) with respect to monthly climatological salinity fields from WOA 2009 yearly average (gray contours at 0.5 PSS-78 intervals). (b) The difference of 2013 and 2012 surface salinity maps estimated from Argo data [colors in PSS-78 yr^{-1} to allow direct comparison with (a)]. White ocean areas are too data-poor to map. While salinity is often reported in practical salinity units, or PSU, it is actually a dimensionless quantity reported on the 1978 Practical Salinity Scale (PSS-78; Fofonoff and Lewis 1979).

oceans (more evaporation in drier locations and more precipitation in rainy areas) as seen in simulations of global warming, which suggest this signal might be discernible since the 1980s (Held and Soden 2006). While anomalous ocean advection could influence the SSS pattern over decadal time scales, changes observed at the local extrema are presumably relatively insensitive to such effects. This SSS anomaly pattern and its interpretation are consistent with other analyses (Boyer et al. 2005; Hosoda et al. 2009; Durack and Wijffels 2010). Changes in ocean interior salinity values also appear consistent with an increase in the hydrological cycle (Helm et al. 2010).

The large relatively fresh patch in 2013 west of Australia and the Indonesian Throughflow (Fig. 3.11a, colors) was also more prominent in 2012 (Johnson et al. 2013b). The strong 2010–12 La Niña, coupled with a negative Indian Ocean dipole and a strong positive southern annular mode, deposited a huge amount of rain on and around Australia in 2010 and 2011 (Fassulo et al. 2013), likely freshening surface waters. La Niña is also associated with an anomalously strong Indonesian Throughflow (England and Huang 2005), which transports relatively fresh waters westward into the Indian Ocean. Most of the rest of the Indian Ocean was saltier than the climatology in 2013.

Sea surface salinity changes from 2012 to 2013 (Fig. 3.11b, colors) strongly reflect 2013 anomalies in precipitation (see Plate. 2.1h) and to a lesser extent year-to-year changes in evaporation, with the latter being closely related to latent plus sensible heat flux changes (see Fig. 3.8d). Advection by anomalous ocean currents (see Fig. 3.17) also plays a role in sea surface salinity changes.

The most prominent large-scale freshening patterns from 2012 to 2013 were in the western tropical Pacific warm pool and along a band in the South Pacific—strongest east of the Solomon Islands, but extending, albeit weakly, to just west of the southern end of South America (Fig. 3.11b, colors). These features are associated with anomalously strong precipitation in 2013 (see Plate 2.1h). The South Pacific feature is also associated with upper ocean cooling (see Fig. 3.5b), and more eastward surface velocity (see Fig. 3.17b) from 2012 to 2013, suggesting influence of a slow down or southward shift of the South Equatorial Current. There was also some freshening under the ITCZ in the eastern tropical North Pacific that is associated with anomalously strong precipitation in 2013 (see Plate 2.1h). In the Indian Ocean, surface salinity increased from 2012 to 2013 in the central equatorial Indian Ocean, possibly owing at least in part to advection by more eastward surface currents (see Fig. 3.17b) and in the Northern Bay of Bengal and Arabian Seas, largely decreasing elsewhere. In addition, while the western Atlantic generally got saltier from 2012 to 2013, the eastern Atlantic generally freshened.

Trends for 2004–13 are estimated by local linear fits to annual average SSS maps (Fig. 3.12a), and are discussed with the ratio of these trends to their 95% significance (Fig. 3.12b). The starting year is 2004 because that is when Argo coverage became near global. Striking trend patterns are found in all three oceans. Saltier surface values in the western and central tropical Pacific extend into the eastern Pacific subtropics in both hemispheres. Large-scale freshening is evident in the eastern tropical South Pacific. Some freshening also occurs in the western subtropics of each hemisphere in the Pacific, west of the Philippine Islands, and in the Indian Ocean northwest of Australia (the latter again perhaps owing to the influence of La Niña over the past few years). The western south Indian Ocean exhibits a trend towards saltier surface salinity values. Much of the Atlantic north of 30°N is

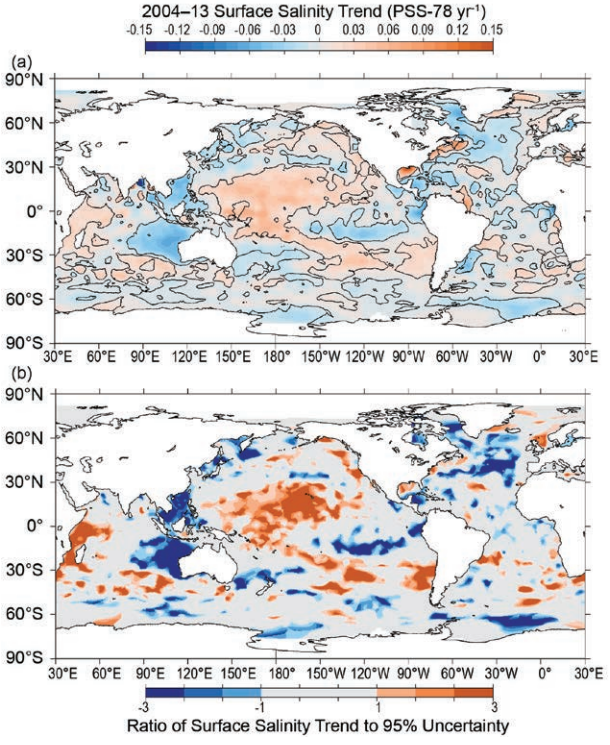

Fig. 3.12. (a) Map of local linear trends estimated from annual surface salinity anomalies for 2004–13 from Argo data (colors in PSS-78 yr^{-1}). (b) Signed ratio of the linear trend to its 95% uncertainty estimate, with increasing color intensity showing regions with increasingly statistically significant trends. White ocean areas are too data-poor to map.

freshening. These trends over the past decade differ somewhat from previously reported multidecadal trends (Boyer et al. 2005; Hosoda et al. 2009; Durack and Wijffels 2010). These differences are not surprising given the different time periods over which the trends are computed.

The patterns of SSS differences of 2013 from 2012 derived from Aquarius data (Fig. 3.13b, colors) are reassuringly similar to those made from the Argo maps (Fig 3.11b, colors); however, in some locations the changes are visibly different in amplitude. The Argo differences also tend to have a bit more variance (on the scale of the Argo mapping and sampling scales) than do the Aquarius differences.

Maps from Aquarius data can be useful for examining the SSS seasonal cycle in detail (Fig. 3.13a); their agreement with Argo climatologies (e.g., Schmidtko et al. 2013) has improved between version 2.0 (e.g., Johnson et al. 2013b) and version 2.8.1 (Fig. 3.13a). Notably, version 2.8.1 exhibits high-latitude freshening from spring to fall that was not evident in version 2.0, and is now in better agreement with the seasonal cycle from Argo. Substantial freshening from March–May (MAM) to September–November (SON) is clear in the western Pacific fresh pool and under the ITCZ across the Pacific and Atlantic as tropical precipitation maxima shift with the seasons. Seasonal salinification just south of the equator in the Pacific is likely owing to mean Ekman advection acting on a seasonally varying salinity gradient (Yu 2011). There is strong salinification in the central tropical Indian Ocean between MAM and SON. Broadscale patterns of salinification between winter and summer in the eastern subtropics (Fig. 3.13a) in both hemispheres are typical of the seasonal cycle and most likely owing to entrainment of fresher water from below in the winter (Johnson et al. 2012b).

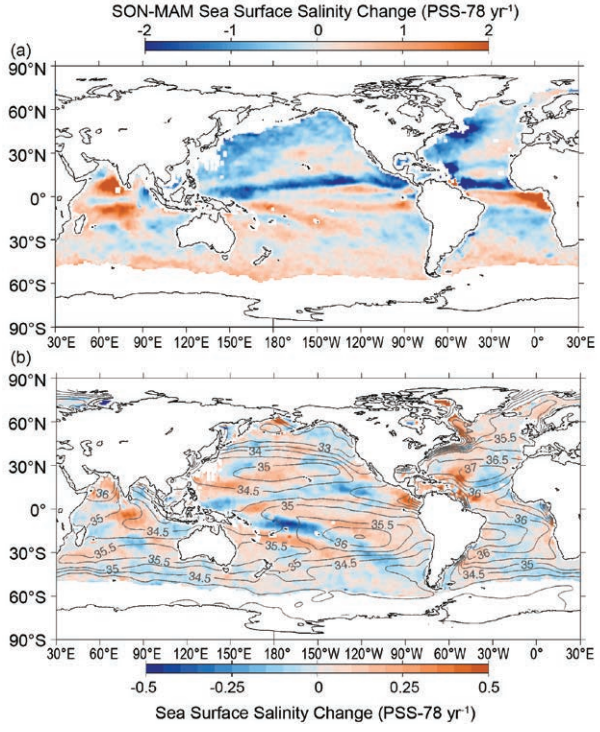

Fig. 3.13. Aquarius V2.8.1 SSS differences between (a) Sep–Nov and Mar–May 2013 monthly maps (colors in PSS-78), and (b) SSS differences of 2013 and 2012 from the means of differences of monthly maps (colors in PSS-78) with WOA 2009 values (yearly average of monthly maps, gray contours at 0.5 PSS-78 intervals) overlaid. White ocean areas have excessive land or ice contamination in the Aquarius field of view.

f. Subsurface salinity—T. Boyer, J. Antonov, J. Reagan, C. Schmid, and R. Locarnini

Evaporation minus precipitation (E–P) is well correlated with mixed layer salinity over much of the world's ocean (Yu 2011). It is difficult to accurately measure evaporation and precipitation over the ocean, so near-surface salinity can be used to constrain E–P estimates (Schmitt 2008; Yu 2011). E–P surface forcing has led to an intensification of the global hydrological cycle over the last 50 years, increasing salinity at the sea surface in areas dominated by evaporation and decreasing salinity in areas dominated by precipitation (Durack and Wijffels 2010; Durack et al. 2012). These surface changes are entrained into the subsurface ocean. Globally, near-surface salt content has increased in recent times compared to long-term averages, while intermediate waters have decreased in salinity (Roemmich and Gilson 2009; Helm et al. 2010). These changes are reflected in changes to ocean water mass composition and circulation patterns. Subsurface salinity changes, along with sea surface salinity (SSS) changes and ocean surface fluxes are important for understanding changes to the ocean and in the atmosphere, both of which affect the global climate system.

To investigate changes to subsurface salinity, all available subsurface salinity profile data for 2013 were used to derive 1° average gridded salinity anomalies at standard depths from the surface to 2000 m. The anomalies were calculated as differences from the 1955–2006 average (Antonov et al. 2010). Differences from recalculated salinity anomaly fields for 2012 are also used to investigate year-to-year variations in salinity. A full description of the method can be found in Boyer et al. (2012).

At present, the single largest source of salinity profiles for the world's ocean is the Argo program with its fleet of profiling floats (Roemmich et al. 2009). From this program, 144 463 salinity profiles were used in the process of calculating subsurface salinity anomalies for 2013. About two-thirds of all float profiles reach 2000 decibars. Because it takes a minimum of six months of data to calculate a final adjustment for salinity drift, less than 10% of the profiles are of the higher level quality-controlled delayed-mode data. For this reason, real-time salinity data with basic quality control were also utilized in this study. Of these, 80 952 profiles include salinity drift adjustments calculated for earlier cycles in a floats lifetime.

In addition to the Argo data, another major source of salinity data is 27 743 daily average profiles from tropical moored buoys (http://www.pmel.noaa.gov/tao/). Included are data from the TAO/TRITON array in the Pacific, PIRATA in the Atlantic, and RAMA in the Indian Ocean, where the deepest measurement was usually at 500-m depth. Almost all buoys are located within 10° latitude of the equator. There also were 14 143 CTD casts largely concentrated in the northwest Pacific and northwest Atlantic and 20 320 profiles from gliders (localized mostly in the Gulf of Mexico, far western Pacific, and northeast Atlantic), most of which were made available through the Global Temperature and Salinity Profile Project (GTSPP). In order to examine the year-to-year change in salinity, anomaly fields for 2012 were recalculated based on updated quality control provided by Argo. A total of 48 558 of the 133 518 Argo salinity profiles recorded in 2012 that were used in this study have now been delayed-mode quality controlled. All salinity and salinity anomaly data were examined using quality control procedures outlined in Boyer et al. (2013a) and are available through the World Ocean Database (Boyer et al. 2013a). All derived fields can be found at http://www.nodc.noaa.gov/OC5/3M_HEAT_CONTENT/. Average salinity anomalies for the upper 100 m at each 1° grid were also computed. The geographic distribution of these fields is similar to SSS fields as presented in section 3e.

The zonally-averaged difference between salinities in the Pacific Ocean in 2013 and the long-term average are shown in Fig. 3.14a. The zonally averaged differences >±0.1 (blue and red shaded areas) in Fig. 3.14a, and subsequent figures, are significant at the 5% confidence level based on Student T tests. Much of the South Pacific was fresher than average in 2013, with the exception of the upper 250 m in the subtropics and along the equator. Below the higher salinity area in the subtropics, freshening was stronger in 2013 than in 2012. Between 50°S and 40°S a freshening relative to average was observed even at depths exceeding 1500 m. Meijers et al. (2011) attribute the freshening in this region to southward movement of the Antarctic Circumpolar Current and water mass changes possibly due to increased precipitation and ice melt. Farther south along the 34.6 isohaline, higher salinity relative to the long-term mean was found. The 2013 salinity anomalies in the South Pacific are comparable to the 2012 salinity anomalies (Boyer et al. 2013b), but with increased salinities reaching deeper in many areas. For example, the area of high salinity south of 50°S in 2013 (Fig. 3.14b) extends to depths greater than 750 m along the 34.6 isohaline near 60°S. Salinity in the upper 100 m (see Fig. 3.11a) shows a large positive salinity anomaly relative to the average under the South Pacific convergence zone (SPCZ), sloping from near the equator in the far western Pacific to around 30°S in the eastern Pacific, similar to 2011 (Johnson et al. 2013b), whereas this feature was weaker in 2012 (see Fig. 3.11b). In the North Pacific, as for 2012, 2013 differed from average with saltier conditions in the upper 250 m near the equator. Freshening at midlatitudes down to 750-m depth, is consistent with the thermocline freshening described by Ren and Riser (2010). Salinity increase exceeding 0.02 occurred in 2013 relative to 2012 below 250 m north of 40°N in the Pacific, including the Bering Sea area. In fact, 2013 salinity in the Bering Sea was similar to 2011 with higher salinity relative

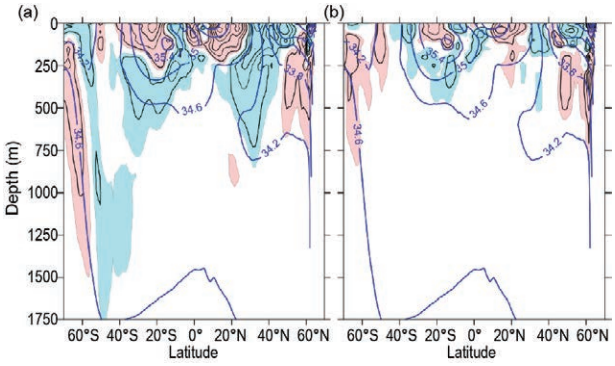

Fig. 3.14. Zonally-averaged (a) 2013 salinity anomaly and (b) 2013 minus 2012 salinity field for the Pacific Ocean. For both figures, blue shading represents negative (fresh) anomalies <-0.01, red shading represents positive (salty) anomalies >0.01. The contour interval for the anomalies is 0.02. In the background of each figure (thick blue contours) is the zonally averaged climatological mean salinity (WOA09). Contour intervals for the background are 0.4. All values are PSS-78 .

to the long-term trend, while a freshening was seen in this area in 2012.

Between the mid-1950s and the mid-1990s an increase in salinity in the subtropical and tropical North Atlantic was coupled with a decrease in salinity in the subpolar North Atlantic (Curry et al. 2003; Boyer et al. 2007; Wang et al. 2010). Since the mid-1990s, both the subtropical and subpolar North Atlantic exhibit increased salinity (Boyer et al. 2007; Wang et al. 2010). This pattern persisted into 2013 (Fig. 3.15a), with the exception of a freshening around 50°N. Most of the North Atlantic increased in salinity in 2013 compared to 2012 in the upper 100 m, with substantial freshening (>0.02) in 100–500-m depth primarily north of about 30°N, in contrast to 2012 where there was freshening over 2011 from the surface to 750-m depth (Fig. 3.15b). Freshening >0.02 extends deeper than 500-m depth around 30°N. This area of freshening expands at shallower depths, with its maximum extent at 150-m depth between 15° and 40°N. At shallower depths, the tropical and subtropical regions of the North Atlantic experienced a large increase in salinity (>0.06). It may be that the freshening signal in the North Atlantic in 2012 was a short-lived anomaly in the decadal signal of increased salinity in the subpolar and subtropical North Atlantic. In contrast to the North Atlantic, the South Atlantic salinity signal in 2013 indicates that the long-term trend was strengthened when compared with the anomalies for 2012. Positive salinity anomalies exceeding 0.06 were found for 2013 down to 250-m depth from 5°–25°S, with anomalies exceeding 0.02 below 500 m south of 20°S. South of 40°S in the Atlantic Ocean, a deep freshening is observed, to depths below 750 m, shoaling to the south, where the freshening is limited to the upper 100-m depth. Between 2012 and 2013, the positive salinity anomalies weakened in the upper 150 m between the equator and 40°S, whereas they strengthened below 150-m depth (Fig. 3.15b). South of 40°S, the trends between 2012 and 2013 were strengthened.

In the Indian Ocean, the differences between 2013 salinity zonal means and the long-term average (Fig. 3.16a) include deep (>1000-m depth) freshening south of the equator, interrupted by increased salinity in the midlatitude south Indian Ocean from the surface narrowing to a maximum depth of 800 m at 40°S. In the upper 100 m (see Fig. 3.11a), the salty anomaly at latitudes north of 30°S is confined to the western half of the Indian Ocean, with freshening in the eastern Indian Ocean. South of 30°S, the positive anomaly extends across the entire basin in a narrow band north of 50°S. The salinity change from 2012 to 2013 in the south Indian Ocean was small (<0.02; Fig. 3.16b), except south of 60°S, where there were limited observations, and just south of the equator in the upper 100 m. Most of the North Indian Ocean zonally-averaged anomalies for 2013 continue to be salty down to depths exceeding 700 m. From 2012 to 2013, changes in the north Indian Ocean larger than 0.02 were mainly confined to the upper 150-m depth and are of the opposite sign when compared with the changes from 2011 to 2012. The fresh anomaly in the upper 100-m depth (see Fig. 3.11b) is less than 0.02 in the central equatorial Indian Ocean, which is smaller than the salty anomaly in the western equatorial Indian. This is the opposite pattern as found between 2011 and 2012. There was a positive Indian Ocean dipole (IOD, east-west temperature gradient >0.5°C) in both 2011 and 2012, but a negative IOD in 2013. It is unclear if there is any relation between the IOD and the upper 100-m average salinity anomaly. In the northern reaches of the Indian Ocean, following the same pattern seen between 2011 and 2012, the eastern Arabian Sea was saltier in 2013 than 2012, while the western Arabian Sea was fresher. Opposite to the

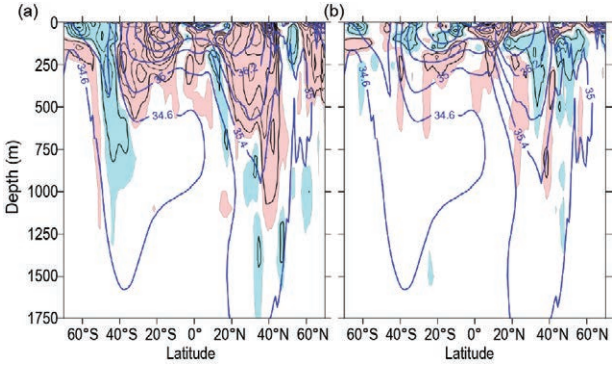

Fig. 3.15. Zonally-averaged (a) 2013 salinity anomaly and (b) 2013 minus 2012 salinity field for the Atlantic Ocean.

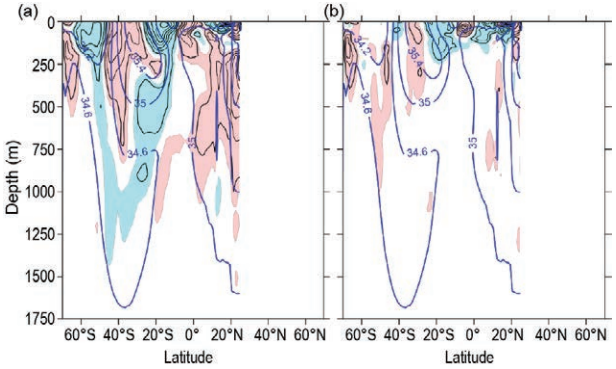

Fig. 3.16. Zonally-averaged (a) 2013 salinity anomaly and (b) 2013 minus 2012 salinity field for the Indian Ocean.

pattern between 2011 and 2012, the northeast Bay of Bengal was saltier in 2013 than 2012, while the rest of the Bay of Bengal was fresher in 2013 than in 2012.

g. Surface currents—R. Lumpkin, G. Goni, and K. Dohan

This section describes ocean surface current changes, transports derived from ocean surface currents, and features such as rings inferred from surface currents. Surface currents are obtained from in situ (global array of drogued drifters and moorings) and satellite (altimetry, wind stress, and SST) observations. Transports are derived from a combination of sea height anomaly (from altimetry) and climatological hydrography. See previous *State of the Climate* reports, from 2011 and before, for details of these calculations. Anomalies are calculated with respect to the time period 1992–2007. Global zonal current anomalies and changes in anomalies from 2012 are shown in Fig. 3.17 and discussed below for individual ocean basins.

1) Pacific Ocean

Compared to the dramatic changes in 2012, 2013 was a relatively quiescent year in the tropical Pacific basin. It began with average January westward surface current anomalies of –25 to –30 cm s^{-1} (negative = westward) across the equatorial Pacific in the band 170°E–90°W, where the climatological westward speed is ~65 cm s^{-1}. By February, these equatorial anomalies had diminished dramatically and were present only in the longitude band 90°–150°W. Throughout the remainder of 2013, no large-scale equatorial anomalies persisted for more than a month.

The eastward North Equatorial Countercurrent (NECC) at 5°–8°N was ~10–20 cm s^{-1} faster than its climatological average from January until August. The longitude of anomalously fast NECC currents shifted westward through these months, located at 90°–140°W in January, 130°–160°W in June, and 130°W–180° in August. These anomalies weakened in September–October, and in November the NECC was close to its climatological strength across the basin.

In March, strong eastward anomalies of 20–30 cm s^{-1} developed at 2°S along 100°–150°W, where the climatological currents are near zero. The location of the anomalies propagated westward and diminished in magnitude through May, located at 150°W–180° in May when they were last seen.

The annual-average zonal current anomaly for 2013 in the Pacific (Fig. 3.17a) highlights the NECC anomalies at 5°–8°N that persisted through most of the year west of the dateline (see above). In the band 145°–170°E, anomalies of 15 cm s^{-1} at 20°N indicated a strengthening of the eastward Subtropical Countercurrent, while anomalies of –15 cm s^{-1} at 22°N corresponded to a strengthening of the westward flow located at this latitude. Alternating zonal bands of ~20 cm s^{-1} anomalies at 33°–36°N, 140°–160°E were consistent with a northward shift of the Kuroshio Extension from its annual climatological position, a shift seen since 2010. For the period 2010–13, the Kuroshio has exhibited a narrower and stronger annual mean signature, shifted approximately 1° in latitude to the north compared to 2006–09. While the climatological latitude of the Kuroshio core at 150°E is ~34.3°N, the core of the current in 2013 was at ~36.0°N, slightly south of the mean position during 2012 (36.7°N). The 2013 minus 2012 map (Fig. 3.17b) is dominated by the strong eastward anomalies that were present in February–August 2012 (Lumpkin et al. 2013).

Surface current anomalies in the equatorial Pacific typically lead SST anomalies by several months, with a magnitude that scales with the SST anomaly magnitude. Recovery to normal current conditions is also typically seen before SST returns to normal. Thus, current anomalies in this region are a valuable predictor of the evolution of SST anomalies and their related climate impacts. This leading nature can

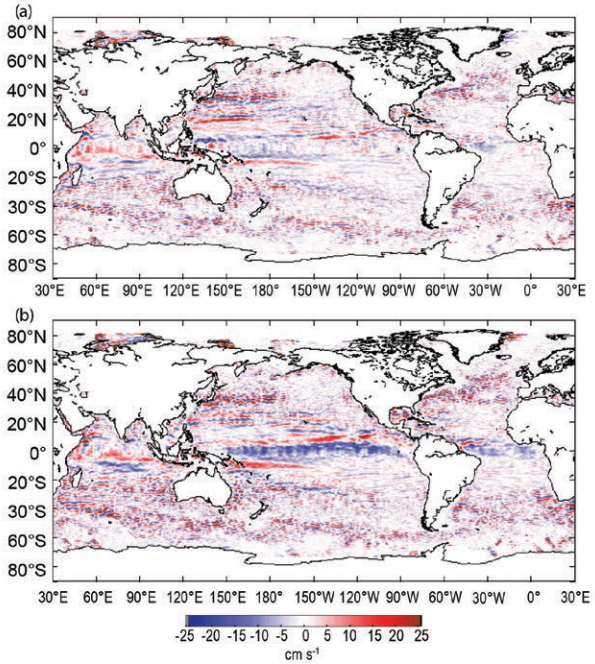

Fig. 3.17. Global zonal geostrophic anomalies for (a) 2013 and (b) 2013 minus 2012, in cm s^{-1}, derived from a synthesis of drifters, altimetry, and winds.

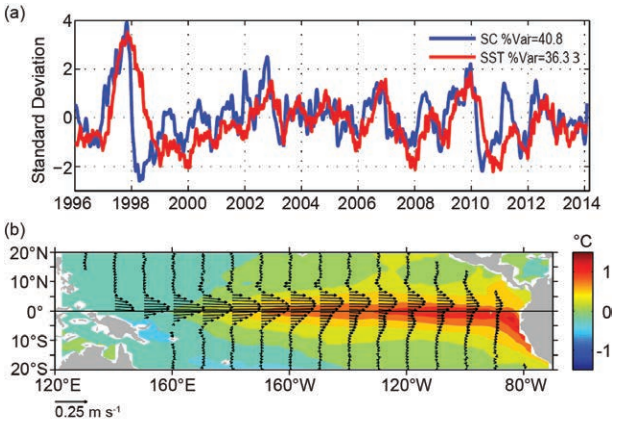

Fig. 3.18. Principal EOF of surface current (SC) and of SST anomaly variations in the tropical Pacific from the OSCAR model (Bonjean and Lagerloef 2002). (a) Amplitude time series of the EOFs normalized by their respective standard deviations for 1996 through 31 Jan 2014. (b) Spatial structures of the SC (vectors, m s^{-1}) and SST (color, °C) EOFs.

be seen in the first principal empirical orthogonal function (EOF) of surface current (SC) anomaly and separately of SST anomaly in the tropical Pacific basin (Fig. 3.18). In the period 1993–2013, the maximum correlation between SC and SST is $R = 0.70$ with SC leading SST by 76 days. Throughout 2013, this mode exhibited weak fluctuations around a slightly negative value for both SC and SST.

2) Indian Ocean

In the western equatorial Indian Ocean, the year began with ~20 cm s^{-1} eastward anomalies over the region 2°S–2°N, 40°–70°E. These anomalies were erased in February–March by the westward equatorial currents that develop during the northeast monsoon season (c.f., Beal et al. 2013). Eastward anomalies were also present in this region in August–November, although they were weaker and not as spatially coherent as in January. Outside this region, at scales larger than mesoscale, surface currents in the Indian Ocean were close to their climatological monthly values until May (i.e., after the northeast monsoon) when eastward anomalies of 15–30 cm s^{-1} developed at 60°–90°E, 2°S–1°N. The climatological May current in this band is 60 cm s^{-1} at 1°S. These anomalies weakened through June–July but remained present, and reintensified in August to 15–20 cm s^{-1}, extending as far south as 8°S in the same longitude band. In October, strong (–20 to –30 cm s^{-1}) westward anomalies appeared at 0°–3°N, 60°–90°E, erasing the pattern of eastward anomalies north of ~4°S (although eastward anomalies persisted at 4°–6°S). These westward anomalies persisted through November. By December, currents

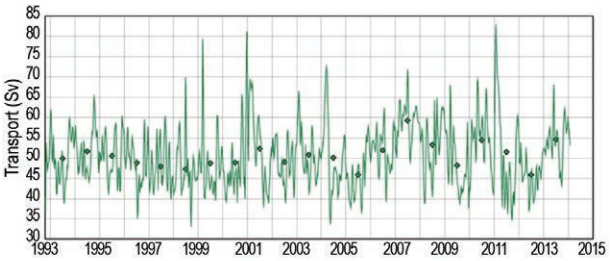

Fig. 3.19. Altimetry-derived transport of the Agulhas Current (Sv) from a combination of sea height anomaly and climatological hydrography. (Source: http://www.aoml.noaa.gov/phod/altimetry/cvar/agu/index.php.)

in the central Indian Ocean basin had returned to their climatological strengths.

The Agulhas Current transport is a key indicator of Indian-Atlantic ocean interbasin water exchanges (Goni et al. 1997). As noted in last year's report, the altimetry-derived annual mean transport of the Agulhas Current (Fig. 3.19) decreased abruptly in mid-2011 compared to its long-term (1993–2013) mean; this reduced transport persisted through 2012 but increased above the long-term average in 2013. In 2012, the annual mean Agulhas transport was ~46 Sv, which (along with 2005) was the lowest annual mean observed since the beginning of the altimetric record in 1993. This increased to an annual average of 54 Sv in 2013, a maximum surpassed only by one year (2007) in the record. Preliminary results indicate that five rings were shed during 2013, which is the average annual value.

3) Atlantic Ocean

In January 2013, currents in the central equatorial Atlantic (6°S–4°N, 5°–30°W) exhibited 10–20 cm s^{-1} eastward anomalies, reversing their direction from the climatological westward flow at ~5 cm s^{-1}. By February these anomalies were present in strength only at the latitude of the NECC, 5°–6°N, while they reduced to <10 cm s^{-1} elsewhere. Eastward anomalies persisted in the NECC until May. In August, westward equatorial anomalies developed across the basin, reaching –20 cm s^{-1} at 2°S in the longitude band 5°–35°W. These anomalies persisted in strength through September and weakened in October–November to ~10 cm s^{-1}, disappearing entirely by December.

During 2013, the velocity fields suggest that the annually-averaged Gulf Stream remained close to its climatological position. This is in contrast to 2012, when large-scale surface current anomalies indicated a northward shift of the Gulf Stream of 1°–1.5° latitude. The North Brazil Current (NBC), which sheds

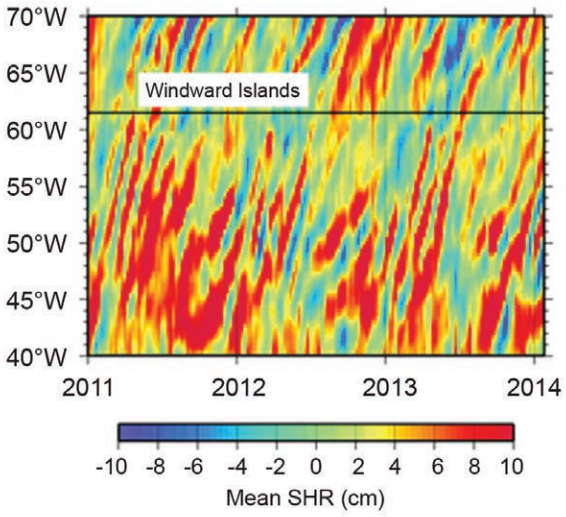

Fig. 3.20. Space-time diagram of de-seasoned sea height residual values (cm) along the NBC ring corridor during 2011–14. (Source: http://www.aoml.noaa.gov/phod/altimetry/cvar/nbc.)

rings that carry waters from the Southern Hemisphere into the North Atlantic basin, exhibited an annual transport close to climatology and shed eight rings, a larger-than-average value (Goni and Johns 2003). Sea height anomalies in the region, which have generally increased since 2001 (apart from the anomalous low years of 2003 and 2008), continued to exhibit higher-than-average values in 2013 (Fig. 3.20).

In the southwest Atlantic Ocean, the Brazil Current carries waters from subtropical to subpolar regions. The separation of the Brazil Current front from the continental shelf break continued to exhibit annual periodicity driven by wind stress curl variations (c.f., Goni and Wainer 2001). However, the annual mean separation of the front was at its average (1993–present) latitude after having exhibited extreme southward anomalies of up to 2° latitude during 2002–11 (http://www.aoml.noaa.gov/phod/altimetry/cvar/mal/BM_anm.php). That southward shift was related to a multidecadal oscillation or was in response to a secular trend in South Atlantic temperatures (c.f., Lumpkin and Garzoli 2010; Goni et al. 2011).

h. Meridional overturning circulation observations in the North Atlantic Ocean—M. O. Baringer, G. McCarthy, J. Willis, M. Lankhorst, D. A. Smeed, U. Send, D. Rayner, W. E. Johns, C. S. Meinen, S. A. Cunningham, T. O. Kanzow, E. Frajka-Williams, and J. Marotzke

The ocean's meridional overturning circulation (MOC) is the large-scale "conveyor belt" that redistributes heat, fresh water, carbon, and nutrients around the globe. Variability in the MOC dominates the variability of transported properties (not variability in the properties themselves), and so the discussion here is focused on the mean and variability of the MOC. For discussion of the importance of the MOC and the state of understanding of this the reader is referred to previous *State of the Climate* reports (e.g., Baringer et al. 2013) and recent reviews such as Macdonald and Baringer (2013), Lozier (2012), and Srokosz et al. (2012). This section reports the results provided by three MOC observing systems in the North Atlantic at 16°N, 26°N, and 41°N.

As part of the 26°N system, the Florida Current (FC, as the Gulf Stream is called at this latitude) has been measured since 1982. Measurements continued through 2013; however, the computer recording system failed twice, leading to two brief gaps in the time series during 28 October–4 November 2013 and during 15 December 2013–3 January 2014. The median transport (from 1982 to 2013) of the Florida Current is 32.0 ±0.26 Sv (standard error of the mean based on an integral time scale of about 20 days) with an insignificant downward trend of −0.25 ±0.28 Sv decade^{-1} (errors using 95% significance with a decorrelation time scale of about 20 days). In 2013 the annual median was 31.7 ±1.7 Sv with the annually-averaged transport essentially equivalent to the long-term average; the 2013 median is within the middle 50% of all annual averages. The daily FC transport values as compared to all previous years (Fig. 3.21a) indicate that 2013 was unusual in that there were several low transport values (extremes defined as outside the 95% confidence limits) during 8–14 March, 10–17 October, and early December. The lowest transport observed (19.7 Sv) occurred on 11 March. This low value was the ninth lowest transport recorded since 1982. During 2013 there was only one high transport event that exceeded the 95% confidence limits: during 10–12 June the transport reached 40.2 Sv.

The RAPID-MOC/MOCHA/WBTS 26°N mooring array continues to provide a twice-daily estimate of basin-wide MOC strength (Fig. 3.22) and is the most complete MOC existing observing system, measuring the full water column across the full basin and absolute transports in boundary currents (see Rayner et al. 2010 for details). McCarthy et al. (2012) noted statistically significant low MOC transport in the winter of 2009/10, showing that the low transport was predominantly caused by both a decrease in the northward Ekman transport and particularly by an increase in the southward interior transport: the overturning weakened as the gyre strengthened. Downturns in the overturning circulation such as

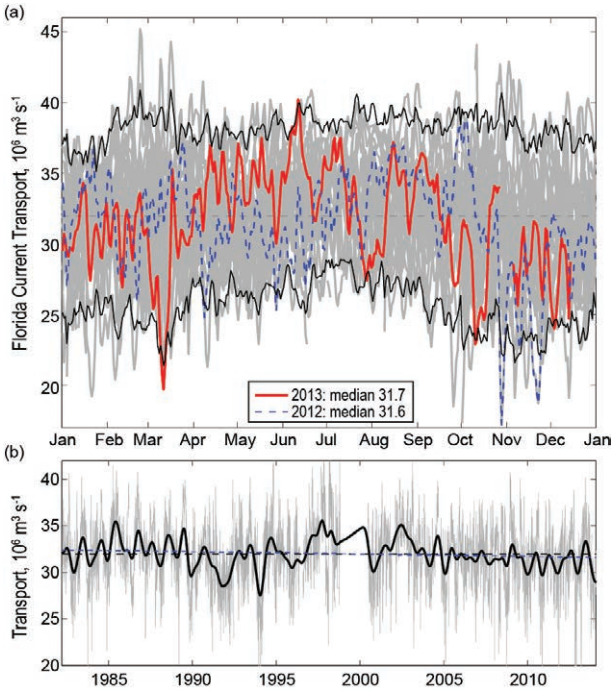

Fig. 3.21. (a) Daily estimates of the transport (×10⁶ m³ s⁻¹) of the Florida Current during 2013 (red solid line) compared to 2012 (dashed blue line). Daily values for years since 1982 are shown in light gray and the 95% confidence interval of daily transport values computed from all years is shown in solid black line; the long-term annual mean is dashed black. (b) Daily estimates of the Florida Current transport (×10⁶ m³ s⁻¹) for the full time series record (light gray), a smoothed version of transport (heavy black line; using a 12-month second-order butterworth filter), the mean transport for the full record (dashed black) and the linear trend from 1982 to present (dashed blue).

this have been shown to cool the subtropical North Atlantic (Cunningham et al. 2013). The MOC and interior transports data (INT) presented in Fig. 3.22 extend the record reported last year from April 2011 through October 2012, while FC and Ekman transport data are available through 2013; MOC estimates based on mooring data require substantially more lead time because a ship is typically required to go to the site to retrieve the data. During this period there was significantly low MOC transport from 4 May to 20 June 2012 (average MOC of 10.8 Sv vs. the long-term mean of 17.3 Sv). The FC contributes about the same reduction during this period as the Ekman transport (about –1.5 Sv), which is half the size of the interior transport contribution (about –3.2 Sv). It is the sum of the Ekman, Florida Current, and interior components that makes up the MOC at this latitude and the 2012 low transport shows a clear dominance of the interior transport changes driving low MOC values. The long-term trend of the MOC is –5.4 ±4.5 Sv decade^{-1} (using 95% confidence assuming a 45-day decorrelation scale); this means there is 95% confidence the decrease in the MOC is greater than 0.8 Sv decade^{-1}. Smeed et al. (2014) examine in detail this downward trend in the MOC and note that the largest changes have occurred since 2008 (as can be readily seen from the annual averages noted on Fig. 3.22).

The 26°N array is not the only array estimating the strength of the MOC in the North Atlantic. At 41°N the MOC in the North Atlantic is being estimated using a combination of profiling Argo floats (that measure the ocean temperature and salinity in the upper 2000 m on broad spatial scales) and altimetry derived surface velocity (see Willis and Fu 2008 for complete details). The data sources for this MOC

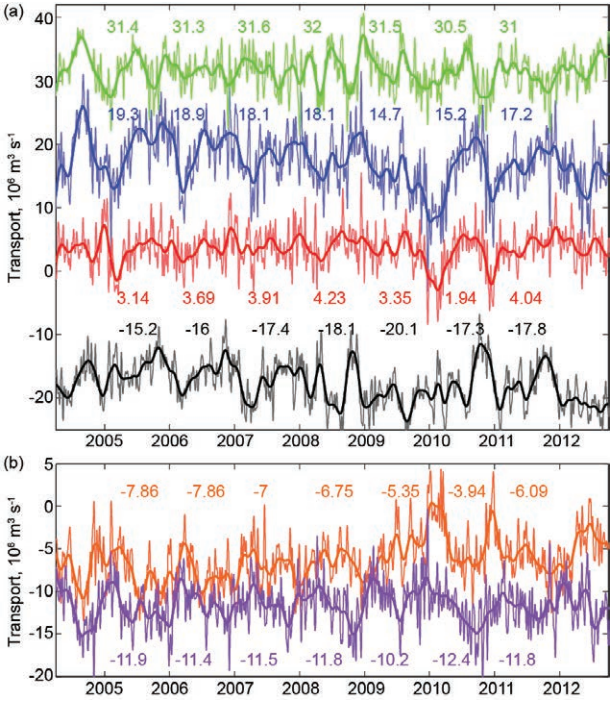

Fig. 3.22. Daily estimates of the (a) strength (×10⁶ m³ s⁻¹) of the meridional overturning circulation (blue line) and its components, the Florida Current (green), wind-driven Ekman transport (red), and the geostrophic interior (black), as measured by the UK National Environmental Research Council (NERC) Rapid Climate Change Program (RAPID-WATCH), the NSF's Meridional Overturning and Heat transport Array proposal, and the NOAA Western Boundary Time Series project (WBTS), and (b) Lower North Atlantic Deep Water (3000–5000-m depth; orange line) and Upper North Atlantic Deep Water (1100–3000-m depth; purple line). The volume transports have a 10-day low pass filter applied to the daily values (Rayner et al. 2010) and the annual averages of the transports for each year are shown in the associated color text (in Sv).

estimate are available in near real-time and hence the time series has been extended from May 2012 (reported last year) to October 2013 (Fig. 3.23). Furthermore, near 16°N, the MOC is being estimated by a mooring array of inverted echo sounders, current meters, and dynamic height moorings that measure the deep circulation that is the southward flowing part of the MOC conveyor belt that sends North Atlantic Deep Water towards the equator (see Send et al. 2011 for further details). For this report, the 16°N data has been updated from June 2011 to October 2013, the date of the last cruise. The updated data from all three latitudes were 90-day low-pass filtered and plotted in Fig. 3.23. The mean MOC based on these estimates decreases to the north (22.8 Sv at 16°N; 17.3 Sv at 26°N; 13.8 Sv at 41°N). Similarly, the variability decreases to the north (as described by the standard deviation: 4.2 Sv at 16°N; 3.4 Sv at 26°N; 2.9 Sv at 41°N). All three time series have a seasonal cycle, which is most prominent at 26°N and 41°N (Fig. 3.23). There are different phases for each, with 41°N having a maximum MOC in May–July, 26°N having a broad maximum in July–November (Kanzow et al. 2010), and 16°N having a maximum southward flow (and hence stronger MOC) in November–January. Of note

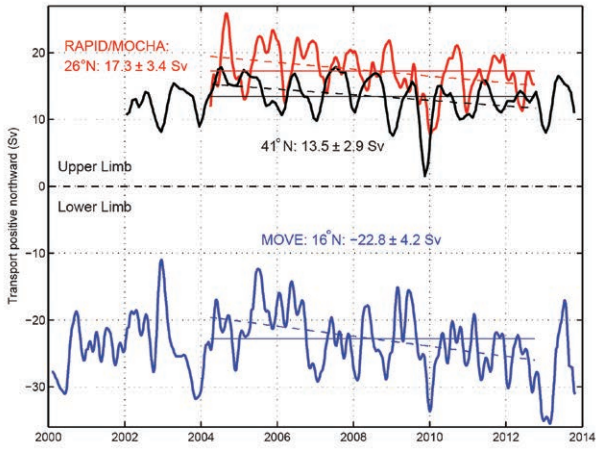

Fig. 3.23. Estimates of the MOC (Sv) in the Atlantic Ocean from the Argo/Altimetry estimate at 41°N (black; Willis 2010), the RAPID-WATCH/MOCHA/WBTS 26°N array (red; Rayner et al. 2010), and the German/NOAA MOVE array at 16°N (blue; Send et al. 2011). All time series have a three-month second-order butterworth low pass filter applied. Horizontal lines are the mean transport during similar time periods as listed in the corresponding text. Dashed lines are the trends for each series over the same time period. For the MOVE data the net zonal and vertical integral of the deep circulation represents the lower limb of the MOC (with a negative sign for the southward flow) and hence a stronger negative southward flow represents an increase in the MOC.

with the most recent data, the 16°N data has stronger southward flow, reaching filtered values above −34 Sv; the new 26°N data is slightly lower than the long-term average and the newest 41°N data is similar to the long-term average. Various authors have reported longer-term MOC trends ranging from zero (Willis 2010 using the first seven years of data from 41°N) to a −3 Sv decade^{-1} decrease (Send et al. 2011 using the first 9.5 years of data from 16°N), to the largest decrease of −5.4 Sv decade^{-1} (Smeed et al. 2014 using the first 8.5 years of data from 26°N). Using the overlapping time period of these observations (2 April 2004 to 2 October 2012) which includes more recent data than reported by Willis (2010) and Send et al. (2011), there is an insignificant trend in the MOC of −3.3 ±6.5 Sv decade^{-1} at 41°N, while at 26°N there is a strong decrease in the MOC of −5.1 ±4.1 Sv decade^{-1} (using 95% confidence limits; Fig. 3.23). However, at 16°N the deep southward flow has recently been increasing, suggesting a possible increase of the MOC at 8.4 ±5.6 Sv decade^{-1}. At 26°N where both the upper and deep southward flows are measured, the decreasing MOC is seen to be compensated by a reduction in the southward export of lower North Atlantic Deep Water (LNADW) in the depth range of 3–5 km (perhaps surprisingly there is no trend in export of upper North Atlantic Deep Water in the depth range 1.1–3 km). The decrease in export of LNADW is 4.6 ±3.9 Sv decade^{-1} (Fig. 3.22b; Smeed et al. 2014). From the full time series from 41°N and 16°N, the MOC trends decrease, becoming insignificant (−0.9 ±4.6 Sv decade^{-1} at 41°N and −2.3 ±2.9 Sv decade^{-1} at 16°N). At these time scales, there appears to be no consistent trend in the MOC at these latitudes. Note that statistically significant changes can be found using various subsets of these time series; however, the interpretation of any trend should consider regional, interannual, and decadal variability that may not be linked to longer-term trends.

i. Meridional oceanic heat transport in the Atlantic Ocean—M. O. Baringer, W. E. Johns, S. Garzoli, S. Dong, D. Volkov, and W. R. Hobbs

The meridional overturning circulation is related to the meridional heat transport (MHT) in the oceans, and the variability of MHT can impact heat storage, sea-level rise, and air-sea fluxes, and hence influence local climate on land. Time series of the oceanic heat transport are more rare than time series of the meridional overturning circulation because they involve the product of temperature and velocity to be resolved across a trans-basin section where

total mass transport can be accounted for. This report includes MHT time series data from 26°N, 41°N, and 35°S in the Atlantic Ocean.

The MHT at 26°N is based on the MOC array of moorings, cabled observations, and Argo profiling float data described in Johns et al. (2011); like the meridional overturning circulation estimates from this array (section 5h), the MHT reported this year has been updated to include new estimates from April 2011 through October 2012. At 26°N the median MHT from April 2004 to October 2012 was 1.25 ±0.36 PW (1 PW = 10^{15} W; Fig. 3.24). The MHT time series follows the general variability of the MOC time series at this latitude. The total MHT is composed of the sum of temperature transports from the Florida Current (median 2.52 ±0.25 PW standard deviation), Ekman temperature transport (0.35 ±0.29 PW), and interior ocean temperature transport (–1.60 ±0.30 PW). The annual median MHT shows a decrease in the MHT in 2009 and 2010 (including negative values in December 2010 for the 10-day low pass filtered data), which then returned to average values in 2011, reported for the first time in this report (Fig. 3.24). The MHT was fairly unremarkable in 2011 and 2012 (Fig 3.24b), except in May and June 2012 when the transport was low for that time of year. For the full time series, the Ekman transport accounts for about 60% of the variance of the MHT (0.77 correlation), while the Florida Current accounts for about 30% of the variance (0.55 correlation). Unlike the MOC, the interior circulation appears to play a lesser role in the variability overall; however, it can be a dominant factor during certain time periods (e.g., McCarthy et al. 2012). The MHT shows a statistically significant decrease of –0.3 ±0.25 PW decade^{-1} (95% confidence limits) from April 2004 to October 2012 (using the full 8.5-year time series); however, this decrease is largely due to the lows in 2009 and 2010 and is likely a signal of interannual and decadal variability rather than a longer-term secular change.

At 35°S in the South Atlantic, MHT has been estimated using a combination of expendable bathythermograph (XBT) data and Argo profiling floats (Garzoli et al. 2012; Dong et al. 2009). From July 2002 to January 2014 the median of the MHT near 35°S is 0.55 ±0.16 PW (±1 standard deviation; Fig. 3.25). At 41°N the MHT was estimated by Hobbs and Willis (2012) using altimetry and Argo profiling float data. The median MHT near 41°N has not been updated since Baringer et al. (2013), and from January 2002 to September 2010 is 0.50 ±0.10 PW. There is no significant trend at 41°N or 35°S, –0.04 ±0.23 PW and +0.12 ±0.12 PW, respectively (Fig. 3.25). The eddy-permitting global ECCO2 data synthesis (Menemenlis et al. 2005) follows nearly exactly the MHT at 41°N, while its average is too low at 26°N and 35°S; however, the correlation is actually highest at 26°N (correlation = 0.8). The state estimation is least correlated with observations at 35°S and has much larger variance in general. Overall, the heat trans-

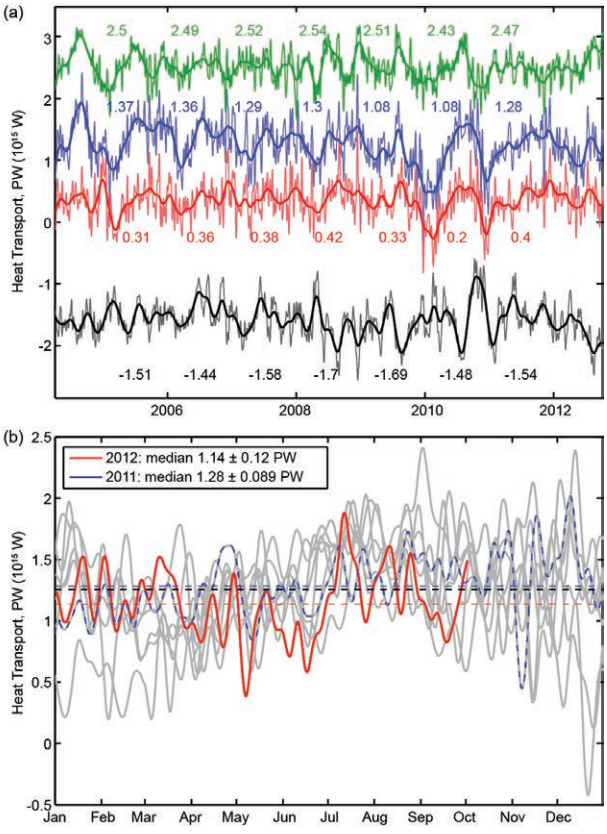

Fig. 3.24. (a) Daily estimates at 26.5°N of the strength (×10^{15} W) of the meridional heat transport (blue line) and its associated temperature transport components, the Florida Current (green), wind-driven Ekman transport (red), and the geostrophic interior (black), as measured by the UK National Environmental Research Council (NERC) Rapid Climate Change Program (RAPID-WATCH), the National Science Foundation's Meridional Overturning and Heat transport Array proposal, and the NOAA Western Boundary Time Series project (WBTS). The high frequency heat transports have a 10-day low pass filter applied to the daily values (Rayner et al. 2010), the smooth curve (heavy lines) represent 90-day low pass filtered data. The annual averages of the transports for each year are shown in the associated color text. (b) MHT (×10^{15} W) from 2012 (red), 2011 (dashed blue), and all other years (gray) plotted as a function of month. Thin horizontal dashed lines are annual mean values for 2012 (red), 2011 (blue), and all years (black).

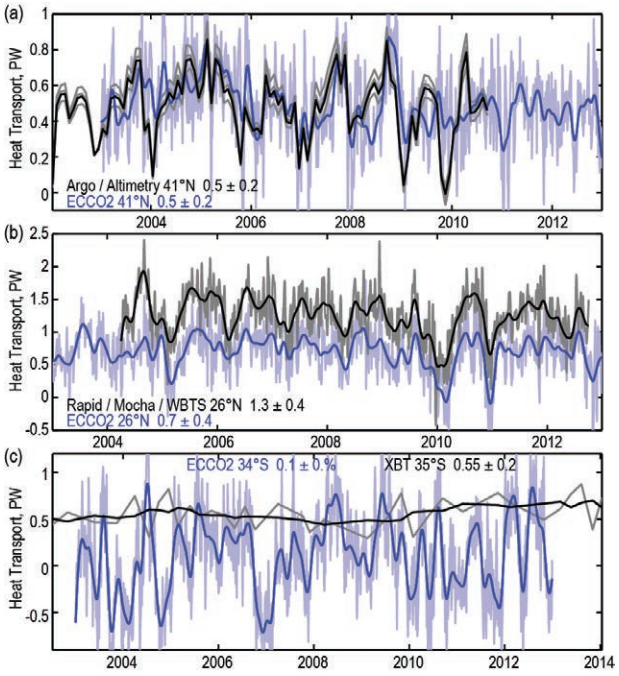

Fig. 3.25. Observed time series of meridional heat transport (PW) at (a) 41°N (profiling floats), (b) 26°N (mooring/hydrography) and (c) 30°–35°S (XBTs) in the Atlantic compared to the monthly estimates from the ECCO2 state estimation (light blue line) and a 3-month low pass of ECCO2 data (blue line). In (a) the black line is the estimate MHT and the gray lines represents the error in the estimate (Hobbs and Willis 2012). In (b) the black line is the observed data filtered with a 3-month low pass filter and the gray lines are the underlying 12-hourly data. In (c) the gray line is the quarterly estimated MHT from XBTs and the black line is a yearly boxcar filter to those quarterly estimates.

port was fairly average in 2012. In 2013, near 35°S the MHT was larger than usual (with August 2013 data falling higher than 97.5% of the other estimates at this latitude).

j. Sea level variability and change—M. A. Merrifield, P. Thompson, E. Leuliette, R. S. Nerem, B. Hamlington, D. P. Chambers, G. T. Mitchum, K. McInnes, J. J. Marra, M. Menéndez, and W. Sweet

Global mean sea level (GMSL) continued to rise during 2013, on pace with a 20-year linear trend of 3.2 mm yr^{-1} (Fig. 3.26a). A portion of this trend (0.5 mm yr^{-1}) has been attributed to natural variability associated with the Pacific decadal oscillation (PDO; Hamlington et al. 2013) as well as to ongoing contributions from the melting of glaciers and ice sheets and ocean warming (Rhein et al. 2013). While interannual variations in GMSL occur regularly, there is no evidence of a hiatus in sea-level rise as has been observed in the surface temperature record over the last decade (Trenberth and Fasullo 2013).

Interannual fluctuations in GMSL about the trend are largely linked to exchanges of water with the continents due to changes in precipitation patterns, including the pronounced minima of 2010–11 and maxima of 2012–13 (Boening et al. 2012; Fasullo et al. 2013). Over 2011–12, global mean sea level rose at ~10 mm yr^{-1} as it recovered from the 2010–11 minima. This is also reflected in the changes in global mean ocean mass measured by satellite gravimetry (Fig. 3.26a) and in global mean continental water storage (see section 2d6). The highest regional sea surface height (SSH) trends occur in the western equatorial Pacific with strong positive trends extending across northern Australia (White et al. 2014, manuscript submitted to *Earth-Sci. Rev.*) and associated weak to negative trends along the eastern boundary of the Pacific (Fig. 3.26b). The regional sea level trend pattern is reflected in the Southern Oscillation and Pacific decadal oscillation indices in the Pacific (Merrifield et al. 2012; Zhang and Church 2012) and northern Australia (White et al. 2014, manuscript submitted to *Earth-Sci. Rev.*) and is a result of multidecadal

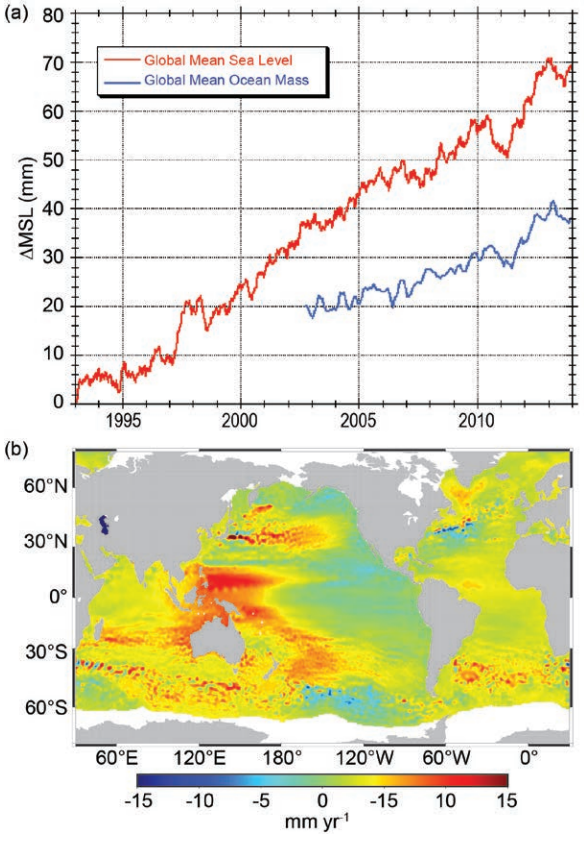

Fig. 3.26. (a) Global mean sea level (mm yr^{-1}) and global mean ocean mass (ppm; seasonal variations removed, 60-day smoothing applied). (b) Regional SSH trends (mm yr^{-1}) 1993–2013.

fluctuations in equatorial and midlatitude winds (Merrifield et al. 2012; Moon et al. 2013).

Maps of SSH averaged over three-month intervals show the anomalous seasonal evolution of regional change during 2013. The positive SSH anomalies around Australia and Southeast Asia during the first half of the year (Fig. 3.27a,b) reflect a moderate La Niña state that relaxed toward an ENSO-neutral state during the second half of 2013 (Fig. 3.27c,d). Positive anomalies in the southeast Indian Ocean persisted throughout the year as anomalies associated with the early-year La Niña conditions propagated westward away from the Australian coast as Rossby waves (Fig. 3.27a–d).

Substantial negative anomalies in the Baltic Sea during the first quarter (Fig. 3.27a) increased steadily to positive values by the end of the year (Fig. 3.27d). This change is linked to a transition from negative to positive phase in both the Arctic and North Atlantic Oscillations. The phase change in these modes also resulted in a moderate decrease of SSH in the Mediterranean Sea (Fig. 3.27a–d). And SSH decreased during 2013 over most of the Southern Ocean (Fig. 3.27a–d). This is most apparent in the South Pacific, where the decreased gradient across the Antarctic Circumpolar Current may reflect the transition from positive to negative values of the southern annular mode.

Annually-averaged sea level during 2013 (Fig. 3.28a) reflects the La Niña-like conditions in the tropical Pacific and Indian Oceans that persisted throughout the year. The PDO index was consistently negative throughout most of 2013, as it has been since mid-2010. The 2013 sea level field is characteristic of a negative PDO phase with low sea level anomalies along the eastern boundary of the Pacific that extend westward across the basin at low latitudes (Merrifield et al. 2012; Zhang and Church 2012). Higher-than-average sea levels at midlatitudes in the northeast Pacific correspond to negative wind stress curl anomalies in the Aleutian Low region (see Fig. 3.9). In the Southern Ocean, the broad region of lower-than-average sea levels west of the southern tip of South America remained essentially unchanged from 2012. Anomalies were positive north of the Gulf Stream and Kuroshio extensions and negative south of these regions, which suggests intensified western boundary currents during 2013. The difference between annual mean SSH maps from 2013 and 2012 shows little change in the large-scale regional features of the SSH field (Fig. 3.28b).

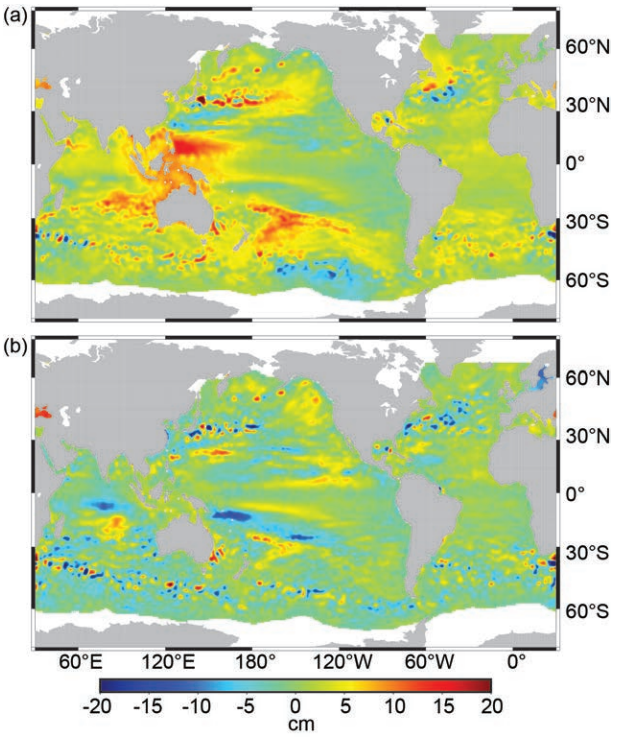

Fig. 3.28. (a) 2013 SSH annual mean anomaly (cm) from the 1993–2012 average. (b) The difference between 2013 and 2012 annual means (cm).

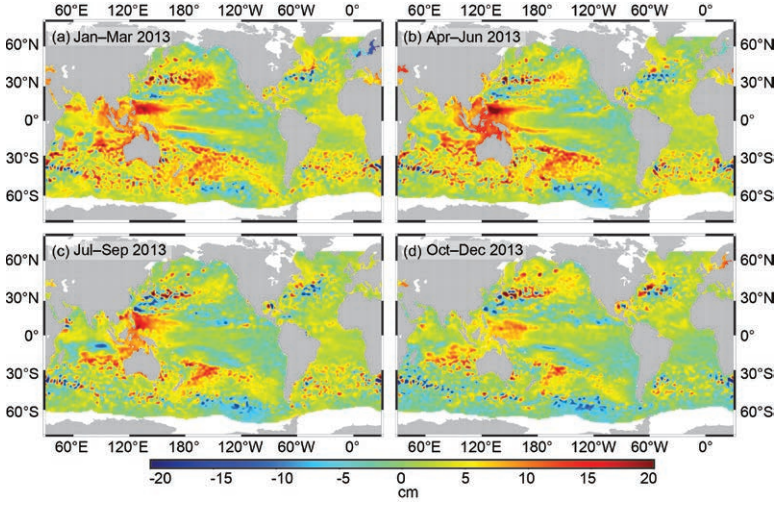

Fig. 3.27. SSH seasonal anomalies (cm) for 2013 relative to the 1993–2012 average, obtained using the multimission gridded sea surface height altimeter product produced by Ssalto/Duacs and distributed by AVISO, with support from CNES (http://www.aviso.oceanobs.com).

Extreme coastal sea levels are examined using daily averages obtained from a global network of tide gauges

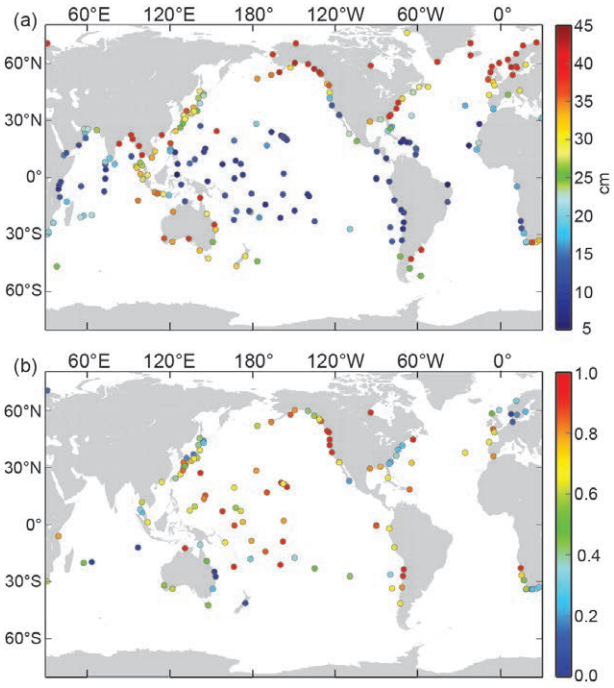

Fig. 3.29. (a) Average of the 2% highest daily-averaged sea level values (mm) from tide gauges. (b) Probability of exceeding the values in panel (a) based on a GEV fit to stations with at least 25 years of data.

(Fig. 3.29a). The average of the upper 2% highest daily values exhibits a characteristic meridional structure that reflects higher storminess at mid- and high latitudes compared to the tropics. The probability of 2013 sea level extremes is estimated by performing a generalized extreme value fit to records with at least 25 years of data. The probability of exceeding the 2013 values (Fig. 3.29b) shows that relatively unusual activity occurred around Scandinavia, parts of Australia and New Zealand, and at scattered island stations in the Indian Ocean. Extremes during 2013 were relatively modest along the western coast of North America and at the majority of tropical Pacific island sites. However, it should be noted that extreme sea levels caused by severe storms such as those associated with Typhoon Haiyan were not well captured by the available tide gauge stations in the Philippines. The issue of the localized nature of extreme sea levels caused by severe storms, such as tropical cyclones, has also been noted for other tropical locations (e.g., Hoeke et al. 2013; McInnes et al. 2014).

k. Global ocean carbon cycle—R. A. Feely, R. Wanninkhof, C. L. Sabine, J. T. Mathis, T. Takahashi, and S. Khatiwala

1) Sea-air carbon dioxide fluxes

The ocean plays an important role in the climate system as a large sink for anthropogenic carbon dioxide (CO_2) and thereby partially mitigates the large-scale effects of human-induced CO_2 emissions into the atmosphere. The air-sea flux of CO_2 is computed from the observed difference in the partial pressure of CO_2 across the air-water interface ($\Delta pCO_2 = pCO_{2sw} - pCO_{2air}$), the solubility of CO_2 in seawater, and the gas transfer velocity (Wanninkhof et al. 2009). Estimates of the net air-sea CO_2 flux based on measurements of partial pressure of CO_2 in near-surface seawater (pCO_{2sw}) and in the marine boundary air show that the extratropics are major oceanic sinks of atmospheric CO_2 and the tropics are major sources (Fig. 3.30). The development of the surface ocean CO_2 maps involves continued processing of the ocean carbon datasets generated from volunteer observing ships and moorings and working with Lamont-Doherty Earth Observatory (LDEO) to update sea-air CO_2 flux climatology (Takahashi et al. 2009, 2013). The process then uses these data along with satellite-based sea-surface temperature and global multiplatform wind products to develop algorithms to make global seasonal CO_2 flux maps.

The LDEO pCO_2 database was used to generate an updated sea-air CO_2 flux climatology in the Regional Carbon Cycle Analysis Project (RECCAP) as reported in Wanninkhof et al. (2013). The gridded pCO_2 dataset was used along with a consistent global wind speed product, the cross-calibrated multiplatform (CCMP) winds (Atlas et al. 2011). Other adjustments to the estimate of Takahashi et al. (2009) include incorporating the impact of El Niño on global sea-air fluxes, a new assessment of sea-ice coverage, and extrapolation of data to the coastline. The updated net sea-air flux is –1.33 Pg C yr^{-1} for the year 2005 climatology

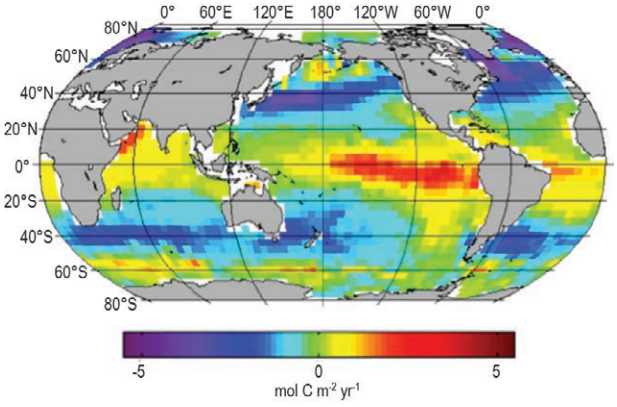

Fig. 3.30. Updated sea-air CO_2 flux (mol C m^{-2} yr^{-1}) climatology yielding a net global sea-air flux of -1.33 Pg C yr^{-1}. The most recent release of the climatological pCO_2 maps centered on the year 2005 can be obtained at http://www.ldeo.columbia.edu/res/pi/CO2/carbondioxide/global_ph_maps/pco2_maps.html.

(Fig. 3.30) compared to the value of –1.22 Pg C yr^{-1} for the 2000 climatology (Takahashi et al. 2009) using the same consistent treatment of ΔpCO_2 fields, gas transfer, and wind speeds. The ΔpCO_2 fields of Takahashi et al. (2009, 2013) with the new wind fields and new gas exchange algorithms are used such that consistent regional and global flux estimates are made over 19 years using the approach of Park et al. (2006, 2010a,b) and Park and Wanninkhof (2012).

Monthly estimates of sea-air CO_2 fluxes and related fields based on the empirical approach of Park et al. (2010a,b) are provided as a user-friendly graphical interface at http://cwcgom.aoml.noaa.gov/erddap/griddap/aomlcarbonfluxes.graph. As an example, boreal summer 2013 (Fig. 3.31) shows a decreased uptake during June 2013 equivalent to 0.4 Pg C yr^{-1} compared to the 30-year average. This anomaly is caused by a combination of larger equatorial outgassing due to enhanced upwelling and decreased uptake in the subpolar gyres as determined from the flux anomaly option of the interface (not shown).

Wanninkhof et al. (2013) recently completed a synthesis of global sea-air CO_2 fluxes and temporal trends from 1990–2009 (Figs. 3.32 and 3.33; Table 3.1). The estimates were based on analyses of ocean inverse models (OIM), atmospheric inverse models (AIM), ocean general circulation models with biogeochemistry (OBGCM), and empirical estimates based on surface water CO_2 observations. The major conclusion is that global ocean CO_2 inventory changes over the last two decades, based on different observational and modeling approaches, show good agreement with an average ocean anthropogenic CO_2 uptake estimate of –2.2 ±0.4 Pg C. The values based on sea-air CO_2 fluxes are on the lower side of the estimates from models and interior estimates. While the magnitude appears well constrained, the interannual variability

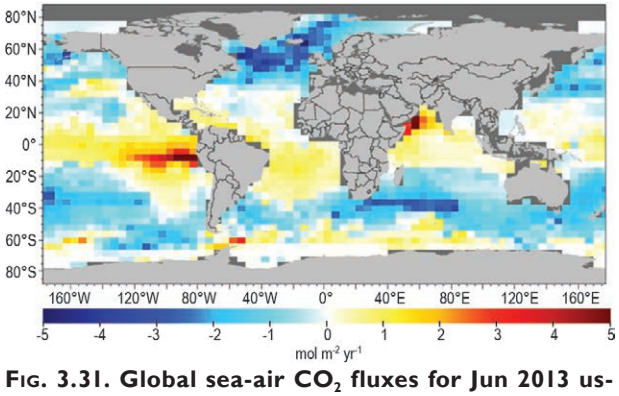

Fig. 3.31. Global sea-air CO_2 fluxes for Jun 2013 using the empirical approach of Park et al. (2010b) and remotely sensed wind and SST data from NOAA Coastwatch.

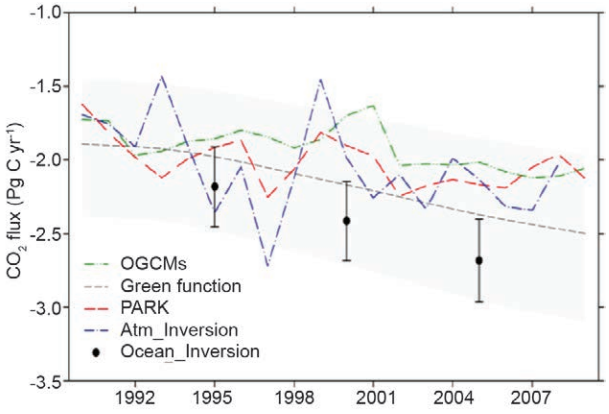

Fig. 3.32. Anthropogenic sea-air CO_2 fluxes based on the empirical approach of Park et al. (2010a) and different modeling approaches from Wanninkhof et al. (2013). The anthropogenic CO_2 flux is the contemporary flux minus the riverine carbon input (≈0.45 Pg C yr^{-1}) where fluxes into the ocean are negative.

and trends between different approaches are quite different, indicating the need for continued work on observational time series.

The interannual variability over the two decades for the OIM and OBGCMs and empirical approaches is approximately ±0.18 Pg C yr^{-1} (Table 3.1). The AIMs showed twice as large interannual variability as the other approaches (≈0.4 Pg C yr^{-1}), which is attributed to incomplete separation of terrestrial and oceanic CO_2 sources and sinks in the AIMs. Consistent differences in the 20-year trend of sea-air CO_2 were observed between methods. Those relying on ocean interior carbon and tracer measurements yielded a

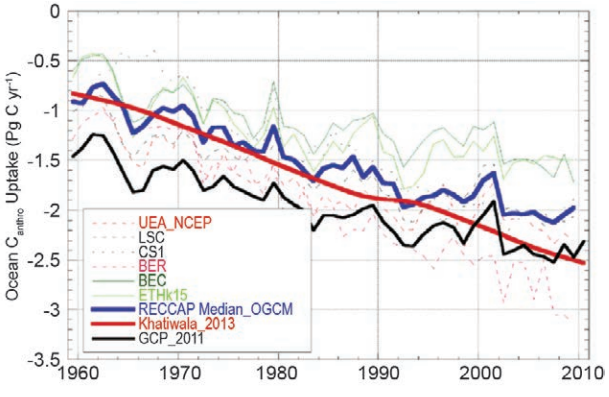

Fig. 3.33. The 50-year globally-integrated ocean anthropogenic CO_2 uptake from coupled ocean biogeochemistry general circulation models (OBGCMs) used in RECCAP. The thin solid and dashed lines show the increasing annual uptake of the different models and their interannual variability. The thick solid blue line is the median of the OBGCMs; the thick solid red line is the output of the Green function method (Khatiwala et al. 2013) and the thick black line is the result from the Global Carbon Project (GCP) ocean model ensemble.

Table 3.1. Magnitude, variability, and trends of sea-air CO_2 using different modeling and empirical approaches centered on the year 2000 (from Wanninkhof et al. 2013).					
Approach	Anthropogenic CO_2 Flux Pg C yr^{-1}	Uncertainty Pg C yr^{-1}	IAV[e] Pg C yr^{-1}	SAV[f] Pg C yr^{-1}	Trend (Pg C yr^{-1}) $decade^{-1}$
Empirical	-2	±0.6[a]	0.2	±0.61	-0.15
OBGCM	-1.9	±0.3[b]	0.16	±0.38	-0.14
Atm. Inversion	-2.1	±0.3[c]	0.4	±0.41	-0.13
Ocean Inversion	-2.4	±0.3[d]			-0.5[j]
Interior (Green function)[g]	-2.2	±0.5			-0.35
O_2/N_2[h]	-2.2	±0.6			
O_2/N_2[i]	-2.5	±0.7			

[a] Root mean square of uncertainty in different components of the flux.

[b] Median absolute deviation of the six model outputs used to determine the median (for six model outputs: LSC, UEA_{NCEP}, CSI, BER, BEC, ETH_{k15}).

[c] Median absolute deviation of the 11 model outputs used to determine the median.

[d] Median absolute deviation of the 10 model outputs used to determine the median.

[e] Interannual variability (IAV) for the median values of the six models list in b.

[f] Subannual variability (SAV) for the median values (for five model outputs: LSC, UEA_{NCEP}, CSI, BEC, ETH_{k15}).

[g] Based on interior ocean changes using transient tracers and a Green function (Khatiwala et al. 2009, 2013).

[h] For 1993–2003 (Manning and Keeling 2006).

[i] For 2000–10 (Ishidoya et al. 2012).

[j] Calculated using steady ocean circulation and CO_2 uptake proportional to atmospheric CO_2 increases.

global trend of increasing carbon uptake ranging from 0.35 to 0.5 (Pg C yr^{-1}) $decade^{-1}$ while those relying on surface water CO_2 values such as OBGCMs and empirical estimates gave values of ~0.15 (Pg C yr^{-1}) $decade^{-1}$. The differences are attributed to the insensitivity of interior measurements to changes in surface biogeochemistry resulting from climate reorganizations and global change. The relatively short time record (two decades) of consistent measurements and model input parameters precludes a definitive attribution of the differences in trends between the different methods.

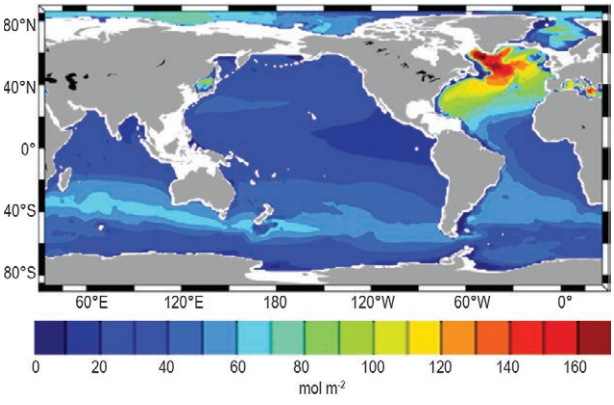

Fig. 3.34. Column inventories for C_{ant} (mol m^{-2}) in 2010. (Source: Khatiwala et al. 2013.)

2) Ocean carbon inventory

The global ocean is continuing to take up a substantial fraction of the anthropogenic CO_2 (C_{ant}) emissions from the atmosphere and, as a consequence, is a significant mediator of global climate change. Estimates based on data-constrained models indicate that the anthropogenic carbon inventory has increased from about 118 ±20 Pg C in 1994 to about 155 ±26 Pg C in 2010 (about 28% of the total anthropogenic CO_2 emissions over that time period; Khatiwala et al. 2013; Fig. 3.34).

The U.S. CLIVAR/CO_2 Repeat Hydrography Program is providing new information about the uptake and storage of carbon within the ocean interior by determining the change in C_{ant} concentration between cruise occupations. Over the last decade, several approaches have been developed to make these determinations using a multiple linear regression method (Friis et al. 2005; Sabine and Tanhua 2010; Clement and Gruber 2014). The effort has continued its basin-wide approach with a focus on the Pacific with a data synthesis project called PACIFICA (see http://cdiac.ornl.gov/oceans/PACIFICA). These data are now being included in the more extensive 2nd Global Ocean

Data Analysis Project (GLODAP-2; Key et al. 2004). In 2013, data from three occupations of the Repeat Hydrography P2 Line in the South Pacific were used to examine changes in dissolved inorganic carbon (DIC) inventories (Fig. 3.35). The changes in DIC are being driven by air-sea exchange at the surface, but also by ventilation processes in the subsurface waters. The high DIC values shown in Fig. 3.35b,d,f between 500 and 1000 m, particularly in the western Pacific, are a result of deep ventilation in these areas. The accumulation of DIC in surface waters is much more pronounced between the 2004 and 2013 occupations due to increasing levels of CO_2 in the atmosphere during that decade. Over the 20-year span of data observations, DIC accumulation in the upper 500 m ranged from <10 μmoles kg^{-1} in the central Pacific to >35 μmoles kg^{-1} in the eastern and western edges of the basin.

The role of the Southern Ocean (SO) continues to be an important factor in understanding the ocean carbon cycle and for predicting future changes in the ocean. A number of recent studies suggest that as much as 40% of ocean uptake of C_{ant} occurs in this region (see Sabine and Feely 2007). However, the amount of C_{ant} that is stored in deep and bottom layers is still uncertain. Significant differences can be found between indirect measurement-based approaches and ocean models (Fig. 3.35). Data from the GLODAP (Global Ocean Data Analysis Project) and CARINA (CARbon dioxide IN the Atlantic Ocean) databases were used to develop a CO_2-data-based "back-calculation" method that provides C_{ant} concentration and inventory estimates in the SO region (>45°S). The method addresses both water mass mixing and the non-steady state nature of the air-sea CO_2 disequilibrium (ΔC_{dis}) term. Water mass mixing was computed using the extended optimum multiparametric (eOMP) analysis. In addition, published parameterizations were used to obtain more reliable values of ΔC_{dis}. Results from the new approach were compared with those from the ΔC^* method, the TrOCA method, and two different tracer-based approaches: the transit-time distribution (TTD) and Green function (GF) methods (Pardo et al. 2014). The TTD, GF, and the new back-calculation methods give similar estimates for the SO inventory (with reference to the year 1994) of 30 ±2, 22 ±2, and 29 ±3 Pg C, respectively (Fig. 3.36). Antarctic Bottom Water shows C_{ant} concentrations of 9 ±1, 3 ±0.3, 6 ±1 μmol kg^{-1}, contributing 6%–12% of the SO inventory. The ΔC^* and TrOCA methods seem to yield lower and higher values, respectively, for both the total C_{ant} inventory and C_{ant} concentrations in deep water layers. Results from the new approach suggest that deep and bottom layers of the water column in the SO contain, in general, low concentrations of C_{ant} compared with subsurface and intermediate layers but higher than those recorded in the global databases. It is important to note that, as deep and bottom layers in the SO fill two of the most voluminous water masses of the global ocean, even these relatively low values of C_{ant} can be of considerable importance when computing the inventories in the water column, mostly in the SO but also in the ocean interior where, over time, bottom waters are moving.

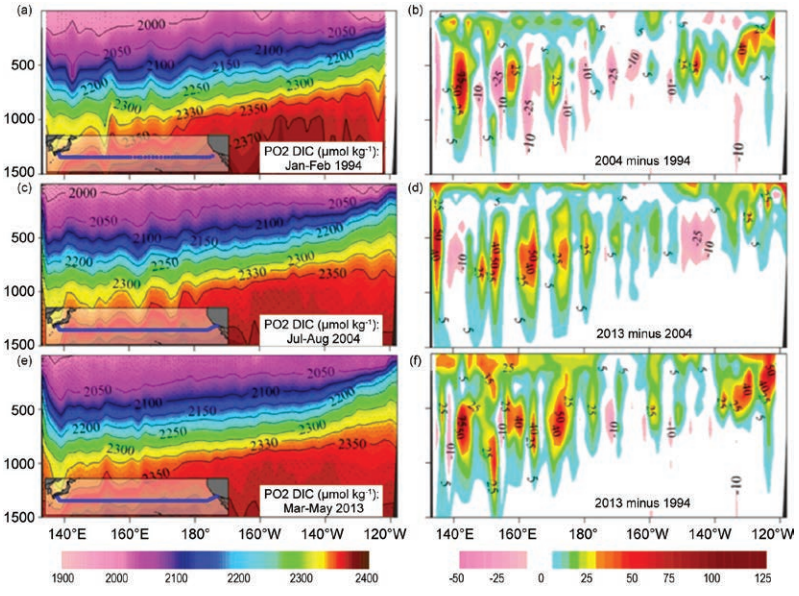

Fig. 3.35. Cross-section of discrete DIC data (μmoles kg^{-1}) from the P02 line taken in (a) 1994, (c) 2004, and (e) 2013. (b), (d), and (f) show the differences in DIC concentrations between the occupations.

The storage rate of anthropogenic carbon dioxide can also be assessed by determining the change in C_{ant} concentration. Large-scale observations of the storage rate are in general agreement with that expected from the increase in atmospheric CO_2 concentrations and with the tracer-based estimates. However, there are significant spatial and temporal differences in the degree to which the inventory of C_{ant} tracks changes in the atmosphere. For example, the subpolar North Atlantic is an area with high variability in circulation and deep water formation, influencing the C_{ant} inventory.

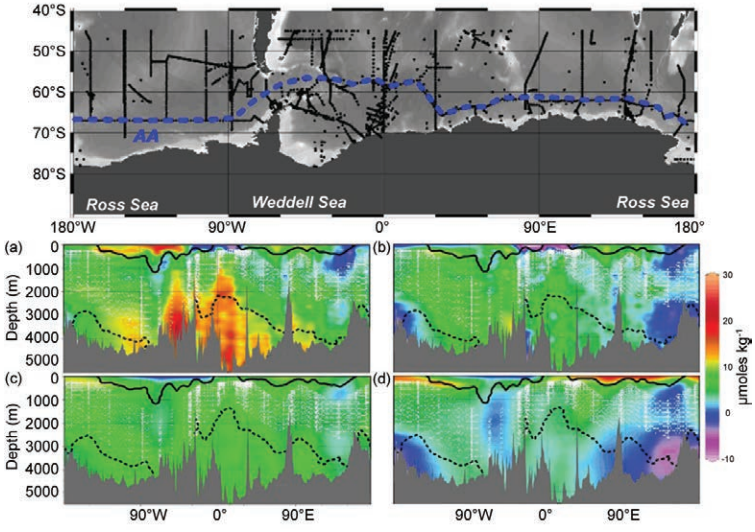

Fig. 3.36. Method dependent estimates of C_{ant} (μmoles kg^{-1}) in the Antarctic Circumpolar Current: (a) TrOCA – ΔC*; (b) C_T^o – ΔC*; (c) TTD – ΔC*; and (d) GF – ΔC*. (Source: Pardo et al. 2014.)

Large differences in storage rates have been observed on decadal and subdecadal time scales (Wanninkhof et al. 2010; Khatiwala et al. 2013).

3) Anthropogenic ocean acidification

Since the beginning of the Industrial Revolution the release of carbon dioxide (CO_2) from human industrial and agricultural activities has resulted in the release of approximately 555 Pg C into the atmosphere (Rhein et al. 2013; Fig. 3.37). During this period, the ocean has absorbed about 155 Pg C from the atmosphere, or a little more than a quarter of the total carbon emissions.

The uptake of excess CO_2 from anthropogenic sources by the ocean lowers the pH and changes the chemical composition of seawater through the thermodynamic equilibrium of CO_2 with seawater. When the excess CO_2 is absorbed by seawater the dissolved CO_2 forms a weak acid (H_2CO_3), which dissociates in seawater such that the pH, carbonate ion (CO_3^{2-}), and calcium carbonate ($CaCO_3$) mineral saturation state ($\Omega = [Ca^{2+}][CO_3^{2-}]/Ksp^*$) of seawater decrease while bicarbonate ion (HCO_3^-) increases (Fig. 3.38). The uptake of CO_2 in the surface ocean results in gradual decrease in the pH of seawater, a process commonly referred to as ocean acidification (Broecker and Clark 2001; Caldeira and Wickett 2003; Feely et al. 2009). Since the beginning of the industrial era there has been a decrease in surface open-ocean pH of 0.1, corresponding to a 26% increase in the hydrogen ion concentration [H^+] concentration of seawater (Orr et al. 2005; Doney et al. 2009; Feely et al. 2009).

The biological consequences of decreases in pH and CO_3^{2-} on marine organisms and ecosystems are only recently being studied in detail (e.g., Orr et al. 2005; Orr 2011; Fabry et al. 2008; Doney et al. 2009; Gattuso and Hansson 2011).

Monthly observations at time series sites reflect changes in both the natural carbon cycle and the uptake of anthropogenic CO_2 from the atmosphere. The observations are based on carbon system and pH measurements at ocean time-series stations in the North Atlantic and North Pacific (Rhein et al. 2013). The results indicate decreasing pH with rates ranging between –0.0014 yr^{-1} and –0.0024 yr^{-1} (Bates 2007; Santana-Casiano et al. 2007; Dore et al. 2009; Olafsson et al. 2009; González-Dávila et al. 2010; Bates 2012). There was good agreement between the long-term pH decreases in the Bermuda Atlantic Time Series (BATS; –0.0019 ±0.0001), European Station for Time Series in the Ocean (ESTOC; –0.0017 ±0.0001), and Hawaii Ocean time series (HOT) at station ALOHA (–0.0018 ±0.0001). Data from the northernmost station off Iceland showed the largest pH decrease (–0.0024 ±0.0002). Directly measured pH differences in the surface mixed layer from a CLIVAR/CO_2 Repeat Hydrography cruise section in the central North Pacific Ocean between Hawaii and

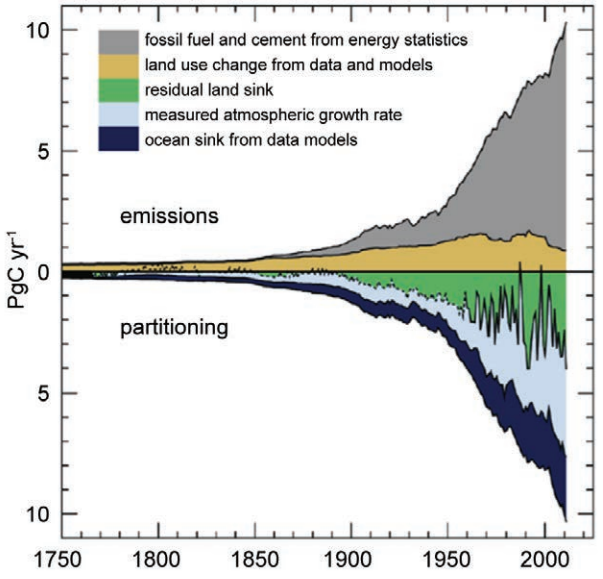

Fig. 3.37. Temporal changes in the partitioning of anthropogenic CO_2 emissions between the atmosphere, oceans, and terrestrial biosphere. (Source: Ciais et al. 2013.)

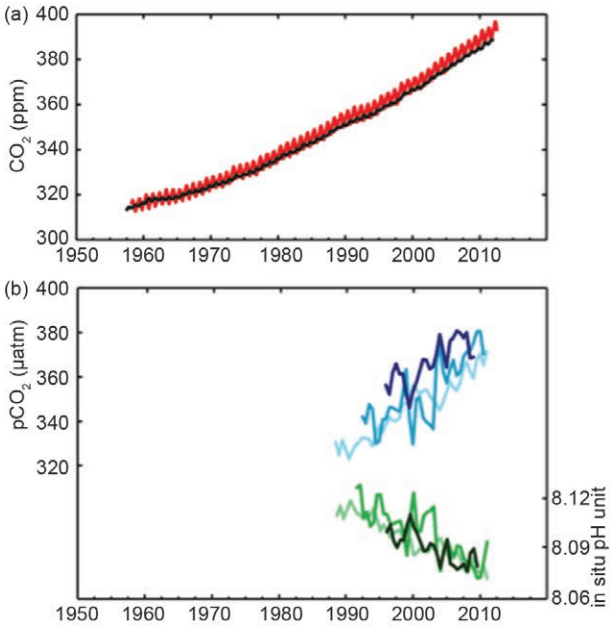

Fig. 3.38. Multiple observed indicators of a changing global carbon cycle: (a) atmospheric concentrations of carbon dioxide (CO_2) from Mauna Loa (19°32'N, 155°34'W; red) and South Pole (89°59'S, 24°48'W; black) since 1958. (b) Partial pressure of dissolved CO_2, at the ocean surface (blue curves) and in situ pH (green curves), a measure of the acidity of ocean water. Measurements are from three stations from the Atlantic (29°10'N, 15°30'W, dark blue/dark green; 31°40'N, 64°10'W, light blue/light green) and the Pacific Oceans (22°45'N, 158°00'W, blue/green) (Source: Alexander et al. 2013.)

Alaska showed a pH decline of −0.0017 yr^{-1} between 1991 and 2006, in agreement with observations at the HOT site (Byrne et al. 2010). This rate of pH change is also consistent with repeat transects of CO_2 and pH measurements in the western North Pacific (winter: −0.0018 ±0.0002 yr^{-1}; summer: −0.0013 ±0.0005 yr^{-1}; Midorikawa et al. 2010). The pH changes in Southern Ocean surface waters are less certain because of the paucity of long-term observations there, but pCO_2 measurements collected by ships-of-opportunity indicate similar rates of pH decrease there (Takahashi et al. 2009).

4) Global ocean phytoplankton—B. A. Franz, M. J. Behrenfeld, D. A. Siegel, and P. J. Werdell

Marine phytoplankton are responsible for roughly half the net primary production (NPP) on Earth, fixing atmospheric CO_2 into food that fuels global ocean ecosystems and drives the ocean's biogeochemical cycles. Phytoplankton growth is highly sensitive to variations in ocean physical properties, such as upper ocean stratification and light availability within this mixed layer. Satellite ocean color sensors, such as the Sea-viewing Wide Field-of-view Sensor (SeaWiFS; McClain 2009) and Moderate Resolution Imaging Spectroradiometer (MODIS; Esaias 1998), provide observations of sufficient frequency and geographic coverage to globally monitor physically-driven changes in phytoplankton distributions. In practice, ocean color sensors retrieve the spectral distribution of visible solar radiation reflected upward from beneath the ocean surface, which can then be related to changes in the photosynthetic phytoplankton pigment, chlorophyll-*a* (Chl*a*; measured in mg m^{-3}). Here, global Chl*a* data for 2013 are evaluated within the context of the 16-year continuous record provided through the combined observations of SeaWiFS (1997–2010) and MODIS on Aqua (MODISA; 2002–present). Ocean color measurements from the recently launched Visible and Infrared Imaging Radiometer Suite (VIIRS; 2011–present) are also considered, but results suggest that the temporal calibration of the VIIRS sensor is not yet sufficiently stable for quantitative global change studies. All MODISA (version 2013.1), SeaWiFS (version 2010.0), and VIIRS (version 2013.1) data presented here were produced by NASA using consistent Chl*a* algorithms.

Annual mean Chl*a* concentrations from MODISA were computed in 4.6 × 4.6 km^2 equal area bins (Campbell et al. 1995) and mapped to an equirectangular projection. The resultant average Chl*a* distribution for 2013 (Fig. 3.39) is consistent with the well-established, physically-driven distribution of

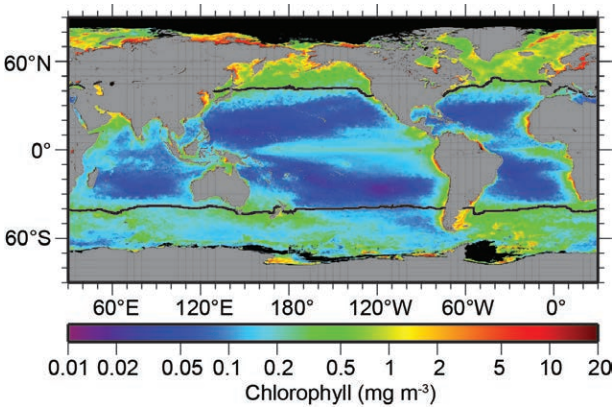

Fig. 3.39. Annual mean Chl*a* distribution (mg m^{-3}) derived from MODISA for 2013. Also shown is the location of the mean 15°C SST isotherm (black lines) delineating the boundary of the permanently stratified ocean (PSO). Chl*a* data are from the NASA Reprocessing of MODISA, version 2013.1. Data are averaged into geo-referenced equal area bins of approximately 4.6 × 4.6 km^2 (Campbell et al. 1995) and mapped to an equirectangular projection centered at 150°W.

nutrients (e.g., Siegel et al. 2013). Chl*a* values during 2013 ranged over three orders of magnitude, from <0.05 mg m^{-3} in the central ocean gyres to >50 mg m^{-3} in nutrient-rich coastal and subpolar waters. Global changes in Chl*a* during this past year were calculated for each geographic bin by subtracting monthly average values for 2013 from values during 2012, and then averaging the monthly anomaly fields to produce an annually-averaged distribution (Fig. 3.40a). Identical calculations were performed on MODISA SST (°C) data to produce an equivalent 2013 SST anomaly (Fig. 3.40b). Positive correlations and inverse correlations between these Chl*a* and SST anomalies are shown in Fig. 3.40c, following the graphical approach of O'Malley et al. (2010). Chlorophyll concentrations during 2013 were also compared to values for the full MODISA mission lifespan (Fig. 3.41). For this analysis, monthly climatological average Chl*a* values (2002–13) were subtracted from monthly values for each year to produce an anomaly time series.

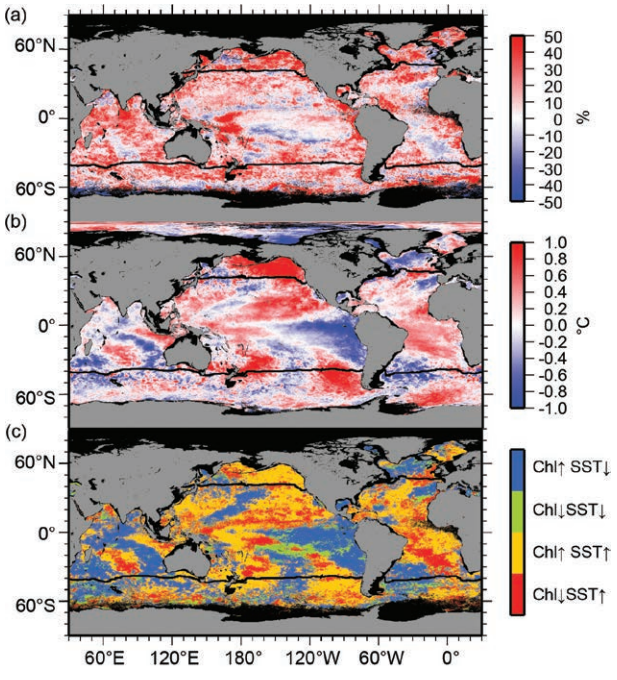

Fig. 3.40. Spatial distribution of summed monthly (a) Chl*a* anomalies (%) and (b) SST anomalies (°C) for MODISA, where monthly differences were derived relative 2012 data. Chl*a* is expressed as % difference from 2012, while SST is shown as an absolute difference. Panel (c) identifies relationships between the sign of SST and Chl*a* anomalies from panels (a) and (b), with colors differentiating sign pairs. Also shown in each panel is the location of the mean 15°C SST isotherm (black lines) delineating the permanently stratified ocean.

In Figs. 3.39 and 3.40, black lines at approximately 40°N and 40°S delineate the relatively stable, permanently-stratified ocean (PSO) from higher-latitude systems, where strong seasonality in surface mixing, temperature, and sunlight drive strong annual plankton cycles. The PSO occupies ~74% of the global ocean surface area, maintains annual-average surface temperatures >15°C, and remains perpetually depleted in surface nutrients (Behrenfeld et al. 2006). Previous studies and annual *State of the Climate* assessments (e.g., Behrenfeld et al. 2006; O'Malley et al. 2010; Siegel et al. 2012) have demonstrated significant inverse correlations between chlorophyll and SST anomalies for the PSO. The expectation for these stratified waters is that a warming sea surface layer is associated with shallower mixing depths, reduced vertical nutrient transport, and higher average mixed layer light levels that together drive decreases in phytoplankton chlorophyll (Behrenfeld et al. 2006). Consistent with these earlier studies, the 2013 versus 2012 anomalies show that regions of decreasing SST (a proxy for stratification) (Fig. 3.40b) were associated with increasing Chl*a* (Fig. 3.40a). The predominance of this relationship is illustrated in Fig. 3.40c by the abundance of blue pixels relative to green. However, the surprising finding for 2013 was that the opposite relationship of decreasing Chl*a* with increasing SST was not equally prominent (i.e., red pixels do not clearly outnumber yellow pixels in Fig. 3.40c). In particular, regions of strong warming across the Pacific were often dominated by increases in Chl*a* (Fig. 3.40c). The reason for this discrepancy from previous years is not clear, but an issue with MODISA Chl*a* retrievals during the past two years cannot yet be ruled out. Regarding this latter possibility, it is noted that: (1) monthly average Chl*a* values during 2012 were at times lower than during the extreme 1998 El Niño year (Fig. 3.41a), yet surface ocean physical properties were not so anomalous during 2012 as in 1998, and (2) the rise in Chl*a* during 2013 (Fig. 3.41a) was expressed throughout almost the entirety of the global ocean (i.e., Fig. 3.40a is predominantly red), which is inconsistent with previous years, including the extreme 1998 event (Behrenfeld et al. 2001).

The multimission record of monthly mean Chl*a* for the PSO, starting with the SeaWiFS mission and extending into the MODISA and VIIRS eras (OBPG 2013), exhibits three primary features shown in Fig. 3.41a: (1) annual maxima in Chl*a* associated with Northern Hemisphere spring–summer phytoplankton blooms; (2) a general offset between MODISA and SeaWiFS data during their 2002 to 2010 overlap

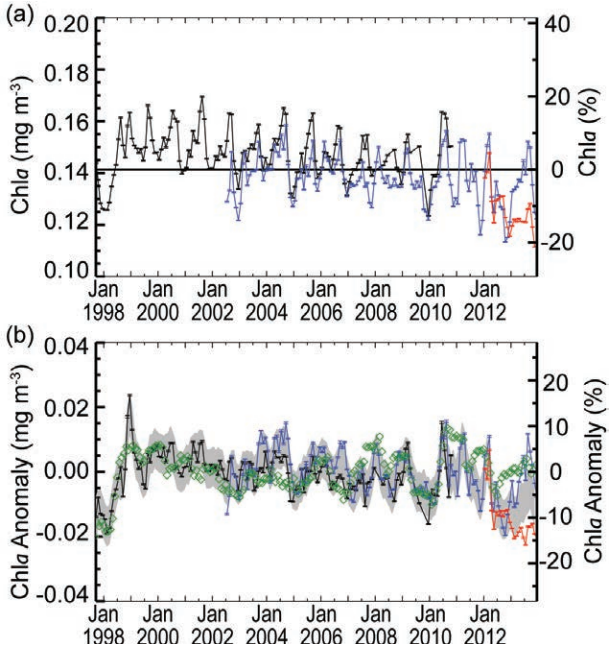

Fig. 3.41. Sixteen-year, multimission record of Chl*a* [mg m^{-3} (left) and % (right)] averaged over the PSO for SeaWiFS (black), MODISA (blue), and VIIRS (red): (a) Independent record from each mission, with horizontal black line indicating the multi-mission mean Chl*a* concentration for the region, and (b) monthly anomaly after subtraction of the monthly climatological mean (SeaWiFS relative to SeaWiFS climatology, MODISA and VIIRS relative to MODISA climatology). The gray region in (b) shows the averaged difference between SeaWiFS and MODISA over the common mission lifetime. Green diamonds show the multivariate ENSO index, inverted and scaled to match the range of the Chl*a* anomalies.

period; and (3) a strong divergence between MODISA and VIIRS Chl*a* for 2013. Regarding the latter feature, the trend in the VIIRS record through 2013 is flat or declining and remains near a historic low. This inconsistent behavior is believed to be due to temporal changes in radiometric performance of the VIIRS instrument that are currently being assessed.

With respect to SeaWiFS and MODISA data, the offset between sensors is essentially eliminated in the time series of Chl*a* monthly anomalies (Fig. 3.41b). Also shown in Fig. 3.41b is the multivariate ENSO index (MEI; Wolter and Timlin 1998), which generally tracks large-scale temporal variability in the monthly mean PSO Chl*a* record (Behrenfeld et al. 2006; Franz et al. 2013). Over the 16-year time series, Chl*a* concentrations in the PSO have varied by ±15% around a long-term mean of approximately 0.14 mg m^{-3}, with largest variations generally associated with El Niño to La Niña climatic events. Mean Chl*a* concentrations in the PSO trended upward from late 2012 to October 2013, for a total increase of approximately 10%, and then declined during the last few months of 2013. This range of variability in MODISA Chl*a* is within the envelope of the long-term record, and the directional character of the trends is consistent with expectations based on the change in MEI, but as previously discussed the magnitude of the change between 2012 and 2013 may not be accurately quantified in the current satellite record. The trend in VIIRS data for 2013, on the other hand, is entirely inconsistent with MEI changes thus adding support for the conclusion that VIIRS trends in 2013 are dominated by instrumental error (Fig. 3.41b). These errors and uncertainties in the 2012 and 2013 ocean color records from MODISA and VIIRS can potentially be reduced as more calibration data are collected and instrument radiometric degradation models are improved, but the results illustrate the caution that must be taken when interpreting ocean color measurements that are so highly sensitive to instrument calibration and characterization accuracy (Siegel and Franz 2010).

Caution is also warranted in the interpretation of satellite-observed temporal trends in Chl*a* concentration as indicators of climate-driven changes in phytoplankton net primary production (Behrenfeld et al. 2008; Siegel et al. 2013). Phytoplankton adjust their cellular chlorophyll content in response to environmental changes in light and nutrient availability, and this physiological response can contribute an order of magnitude variability in Chl*a* that can dominate monthly to interannual variations in PSO anomalies. As such, changes in the satellite time series can either reflect physiological variability or changes in abundance, with these two sources of variability having strongly divergent implications on NPP. Interpretation of the Chl*a* record is also complicated by limitations in the ability to separate optical signals of phytoplankton abundance from colored dissolved organic matter, which is simply assumed to co-vary in the traditional band-ratio algorithms employed here (e.g., Siegel et al. 2013).